A Viral Toolkit for Ultrasound Imaging of Cellular Activity and Gene Expression

Thesis by
Shirin Shivaei

In Partial Fulfillment of the Requirements for
the degree of
Bioengineering

CALIFORNIA INSTITUTE OF TECHNOLOGY
Pasadena, California

2025
Defended February 4, 2025

Shirin Shivaei
ORCID: 0000-0002-6894-3289

ACKNOWLEDGEMENTS

Without mentorship, the wisdom of one generation may never reach the next. I want to begin by thanking my academic mentors who have believed in me as a scientist and have given me the space to explore and discover my scientific identity. First of all, my PhD advisor, Mikhail Shapiro, whose enthusiasm, energy, and optimism are inspiring. Mikhail gave me one of the most valuable things early in graduate school: independence and the freedom to work on some of the highest-stakes projects in our lab. His trust in me to deliver on these projects has been a priceless part of my PhD and essential to shaping my scientific personality.

I also want to thank my advising committee: Michael Elowitz, for always bringing a fresh perspective to the table and pushing me to think deeper about different scientific questions; Mickael Tanter, for enthusiastically helping me come up with new ways of processing ultrasound data; and Yuki Oka, for his deep and much-appreciated perspective as a neuroscientist.

I am also grateful to my master's advisor, Fei Chen, who trusted me enough to take me into his lab as an undergraduate from a completely different academic background in EECS. Working with Fei and the rest of the "In Situ Biology Team" was truly the beginning of my career in the field of biomolecular engineering, and perhaps one of the most pivotal moments in helping me find my true scientific passions.

Scientific progress is never a solitary adventure, so I want to thank Shapiro Lab members for always being there to lend me a hand, no matter the time of day, and for creating one of the most dynamic and interdisciplinary spaces to work in. Especially Ann Liu, for not just providing help with my project but also for also her selfless commitment to doing day-long experiments with me while making it fun with snack deliveries; Kathy Cheung, for her expert help with brain surgeries and for being my personal coffee barista on campus; Claire Rabut, for always making work fun and for letting me show her synthetic biology while teaching me ultrasound imaging; Akanksha Yadav, Ernesto Crialdo-Hidalgo, and Pierina Barturen for their help with some of my hardest and most hands-on experiments; Zhiyang Jin, Bill Ling, and Marjorie Buss, for generously helping me troubleshoot experiments; Avinoam Bar-Zion and Di Wu, for including me in their projects during the early days of my PhD; Abdullah Farooq, for never failing to make me laugh; my former undergraduate mentee, Bella Hurvitz, who always astonishes me with her ability to learn so fast; and Julio Revilla, without whom the final push to finish the two vastly different projects I was working on would have been

much more difficult. Everything I have accomplished in the Shapiro Lab is thanks to the amazing colleagues I've had.

Pursuing a PhD is a long journey, and it's the community around you that makes it bearable and joyful. I want to thank my roommate, Linlin, who started this journey with me. We shared our moments of despair and happiness together—over many bowls of noodles, playing games, weekend escapes to mountain cabins, exploring the mountains of Hawaii, and countless other memories that I will cherish forever. And my other roommate, Khalil, and our two cats, Titto and Nimbo, for making our house a place that truly feels like home.

I was lucky to make some truly wholesome friendships during my time at Caltech. Among them were Claire and Aaron, my DTLA getaway hosts, who were always there to celebrate with me—whether it was my birthday or my defense, and Kathy who revived my passion for climbing. In a happy coincidence, I also met an incredible group of Iranian friends at Caltech during my later years of graduate school: I want to thank Bahareh, who reminded me that it's okay to break norms—I'll miss our bike rides; Yasamin, for our long conversations about life over coffee; Termeh, for her energy and determination that brought all of us together; and Golsa, Mina, and the rest of the friend group for creating a community I felt I had left back in Iran. I'm especially thankful for our Thursday poetry nights, which reintroduced me to Persian poetry—a part of my Iranian heritage I had long been separated from.

Beyond the borders of LA, I want to thank my MEng roommates—Erin, Suma, and Deepti—who, despite the distance, have always stayed in touch and I will always look up to. And to Sayna, for sharing our quirky love of nature and reminding me to slow down and enjoy the world around me.

None of this would have been possible without the support of my aunt, Khaleh Mansoureh, who enabled my family's immigration to the USA, took me on tours to colleges around Boston and opened a world of opportunities to me. I also want to thank Negar Joon and Daee Sasan, who warmly welcomed me into their home and were my base in Cambridge as I figured out life in a new country as a college student. The Heidarzadeh and Mobasher families, for always encouraging me and celebrating my accomplishments—from my college admissions all the way to my PhD. The Abedi family, for always treating me as one of their own. The Atashrazm and Jamshidi families, who, no matter how long it has been since I last saw them, make it feel as if no time has passed. Special thanks to Nasrin Khanoom, who, when I was in high school, encouraged me to consider bioengineering as

my college major. And my family in Iran, who have always supported me from far and near—particularly my aunt Ame Zari, whose timeless words of wisdom during our weekly phone calls always unlock a new perspective for me in life.

It is perhaps hardest to thank the people dearest to me, as words do not suffice to show the extent of my gratitude. To my partner, Mohamad—every time I felt low, you believed in me and reminded me not to take life too seriously. To my sister, Irene, who—whether consciously or not—has always been my role model, I learned from you what it means to live life to its fullest. I can't imagine what course my life would have taken without your example. To Tim, thank you for being by our side and always present for our family occasions. To my Maman, the most inspiring and strongest woman I know—you've shown me that it's possible to make space for the things you care about in life without sacrificing your career and ambitions. To my Baba—you taught me how to think critically and helped me see that knowledge is not enough; that true understanding comes from wisdom. To my family—It is perhaps because of you that I found my way to this challenging yet fulfilling path, and for that, I am forever grateful.

ABSTRACT

Observing and manipulating cell dynamics in living organisms is essential for understanding biological processes and intervening when they malfunction. However, the lack of non-invasive, non-ionizing, and cost-effective imaging technologies limits our ability to study these processes in their native context. To address this gap, we developed a toolkit for ultrasound imaging of acoustic reporter gene expression in mammalian tissues using virally-delivered gas vesicle (GV) genes. We demonstrate the versatility of this toolkit across multiple applications, including tracking engineered cell-based therapies and imaging activity-dependent gene expression in the brain.

To track cell-based therapies, we developed lentiviral vectors encoding the eight genes necessary for GV expression, achieving robust ultrasound contrast in both cell lines and primary human T cells. By expressing GVs downstream of NFAT-dependent promoters, we monitor T cell activation in cytotoxic T cells engaged with tumor cells. In a mouse xenograft model, we then image the targeted accumulation and proliferation of GV-expressing T cells within tumors. These ultrasound measurements, which closely correlate with immunohistological analysis, provide real-time, in vivo insights into the spatial dynamics of therapeutic cells. This approach offers a powerful tool to accelerate the development and clinical translation of cell-based therapies.

We extend this technology to the brain by engineering an AAV-based system for GV expression in primary neurons. Following intracranial injection of the GV-encoding AAVs in mice, we demonstrate longitudinal imaging of in situ gene expression in the brain of the same animal over several weeks. Moreover, by using immediate early gene promoters to drive GV expression, we track changes in neuronal activity in the hippocampus during seizure episodes, enabling repeated, longitudinal imaging of brain function within the same animal. Collectively, these advancements establish a robust platform for real-time ultrasound imaging of cellular activity and gene expression in opaque tissues, with applications ranging from cancer immunotherapy to neuroscience.

PUBLISHED CONTENT AND CONTRIBUTIONS

Sawyer, D.P., Bar-Zion, A., Farhadi, A., **Shivaei, S.**, et al. Ultrasensitive ultrasound imaging of gene expression with signal unmixing. *Nat Methods* **18**, 945–952 (2021). https://doi.org/10.1038/s41592-021-01229-w

Contributions: S.S. prepared genetic constructs in HEK293 cells, performed flow cytometry measurements, and provided input on the manuscript.

Bar-Zion, A., Nourmahnad, A., Mittelstein, D.R., **Shivaei, S.**, et al. Acoustically triggered mechanotherapy using genetically encoded gas vesicles. *Nat. Nanotechnol.* **16**, 1403–1412 (2021). https://doi.org/10.1038/s41565-021-00971-8.

Contributions: S.S. designed, planned, and conducted the mammalian *in vitro* experiments. S.S. also provided input on the manuscript.

Wu, D., Baresch, D., Cook, C., Ma, Z., Duan, M., Malounda, D., Maresca, D., Abundo, M.P., Lee, J., **Shivaei, S.** et al. Biomolecular actuators for genetically selective acoustic manipulation of cells. *Science Advances*, *9*(8), p.eadd9186 (2023). DOI: 10.1126/sciadv.add9186

Contributions: S.S. designed, planned, and conducted the mammalian cell experiments. S.S. provided input on the manuscript

Shivaei, S., Liu, A., Abedi, M.H., Revilla, J., Hurvitz, I.U., Swift, M.B. and Shapiro, M.G.. Non-invasive imaging of cell-based therapies using acoustic reporter genes. *bioRxiv*, pp.2024-11 (2025). DOI: https://doi.org/10.1101/2024.11.01.621111

Contributions: S.S. conceived and planned the study, conducted experiments, analyzed resulting data, and prepared the manuscript.

Shivaei, S., Cheung, K.Y.M., Yadav, A., Hurvitz, I.U., Lee, S., Revilla, J., Rabut ,C., Crialdo-Hidalgo, E., Zhang, R., Shapiro, M.G. 2025. Deep-tissue ultrasound imaging of in situ cellular function using acoustic reporter genes. In preparation.

Contributions: S.S. conceived and planned the study, conducted experiments, analyzed resulting data, and prepared the manuscript.

Shivaei, S., Mikhail G Shapiro, Viral delivery of gas vesicle genes. March 30, 2023. Patent application, ID US20230094152A1.

TABLE OF CONTENTS

LIST OF ILLUSTRATIONS AND/OR TABLES

C h a p t e r 1

VISUALIZING CELLULAR FUNCTION DEEP INSIDE THE BODY

1.1 Seeing is believing

Biological discoveries over the last century owe much to our ability to visualize biological structures and processes with high spatial and temporal resolution. Breakthroughs such as the discovery of the DNA double helix with X-ray crystallography, visualizing dynamic changes of subcellular processes with optical microscopy, mapping cellular organelles with electron microscopy, functional mapping of brain activity in humans with magnetic resonance imaging (MRI), the visualization of human fetus with ultrasound, a few examples among many, have all been made possible by advancements in imaging technology.

Many of these discoveries were enabled by the development of high-resolution optical objectives and new optical imaging techniques, such as confocal imaging and light sheet microscopy. However, there remains a fundamental limitation: visible light does not penetrate deeply enough into tissue to allow us to observe cells and their function in their native context. To overcome this, we turn to alternative imaging modalities that, while they might not offer the same micrometer resolution as optical imaging, can penetrate deeper into tissues, allowing us to visualize biological processes *in vivo*.

Several imaging modalities, including positron emission tomography (PET), MRI, and ultrasound, provide such capabilities. While each modality has its strengths, ultrasound stands out for several reasons. Compared to MRI and PET, ultrasound offers superior spatial resolution, on the order of 100 μm[1], with advanced super-resolution ultrasound techniques achieving higher resolutions[2]. Moreover, ultrasound is portable, and its equipment is significantly more affordable and easier to maintain than that of MRI and PET. In contrast, risks associated with radioactivity and the short half-life of PET tracers make their use more challenging. These advantages of ultrasound position it as a particularly attractive tool for *in vivo* imaging.

Just as the development of optical imaging technologies revolutionized biological research, the invention of fluorescent proteins, such as GFP, enabled us to visualize molecular processes within living cells. The concept of reporter genes has further empowered this approach, allowing researchers to track gene expression and cellular activity. A similar concept has emerged with the development

of gas vesicles (GVs)—hollow, air-filled protein nanostructures naturally found in cyanobacteria—that have been engineered as the first acoustic reporter genes (ARGs). The ultimate goal is to not only achieve what is possible in cell culture with optical imaging, but to go beyond and use acoustic reporter genes to track and visualize cellular activity *in vivo*, within the complex and dynamic environment of living organisms.

1.2 Advancing biological discoveries with ARGs

In the past decade, there has been remarkable progress in the development of gas vesicles (GVs) as acoustic reporter genes. Following their first demonstration in ultrasound detection[3], recombinant GVs have been expressed in bacteria[4] and have been successfully used for applications such as localizing probiotic bacteria in the gut[5,6] and as cavitation nuclei for targeted cell killing and drug delivery[7]. Additionally, novel techniques have been developed, such as acoustically sorting cells based on their GV expression[8]—analogous to flow cytometry based on fluorescence expression. Furthermore, we have developed highly sensitive methods for imaging GVs, such as BURST imaging and xAM[9,10], that increase signal-to-background ratio by taking advantage of the nonlinear scattering of GVs and reducing background signal. Most notably, GVs have been successfully expressed in mammalian cells[5,11]. Recent advancements have focused on developing smaller gene clusters that significantly reduce the DNA footprint, making GV expression more efficient and easier to integrate into mammalian systems[12,13].

Despite these advancements, challenges remain in taking this technology to the next level of widely accessible genetic tools, where it can be used as routinely as fluorescent proteins. One key issue is equipment availability: while nearly every biology lab has access to a microscope, not all labs have access to an ultrasound system. However, there is a more fundamental challenge that needs to be addressed to reduce the barrier to GV technology. Fluorescent proteins, such as GFP, only require a single gene for expression, whereas the smallest GV gene cluster expressed in mammalian cells, consists of 8 genes and occupies approximately 4.5 kb of DNA space—much larger than the ~600 bp footprint of GFP. In addition to the size of the cluster, fine-tuning the stoichiometry of these genes to ensure optimal expression while avoiding over-expression is complex.

Although co-expressing the 8 GV genes in immortalized cell lines like HEK cells may be relatively straightforward through transient transfections, expressing them in primary cells or *in vivo* systems, which better reflect human biology, presents a significant hurdle. In this work, we demonstrate how careful design of viral vectors has enabled the efficient delivery of the GV gene cluster into primary

cells of various types. With this toolkit, any lab with access to an ultrasound system should be able to engineer desired cell types or directly inject the viral vectors into living organisms, providing a new means of non-invasive visualization.

There are two particularly promising contexts where mammalian ARGs could make a significant impact: 1) in visualizing immunotherapies to better understand their complex dynamics *in vivo*, and 2) in enabling non-invasive imaging of brain function at a whole-brain scale.

1.3 Tracking cell-based therapies with ARGs

The combination of synthetic biology and immunotherapies has led to significant advancements in cancer treatment, as seen with technologies such as CAR-T cell therapies. While these therapies have shown promise, particularly in treating B cell lymphoma with CD19-targeted CAR-T cells, there are still complex *in vivo* dynamics that are not fully understood and thus difficult to predict. For example, the core of solid tumors is difficult to access, and the extent to which engineered cell therapies reach the tumor core varies greatly between patients. Tumor heterogeneity, both in terms of cellular composition and the tumor microenvironment, further complicates the ability of therapeutic cells to effectively target and eliminate tumor cells. Another challenge is the risk of on-target, off-tumor cytotoxicity, which can be fatal. Off-tumor toxicity arises when CAR-T cells attack healthy tissues that express the target antigen, leading to severe side effects. Additionally, immune escape mechanisms employed by tumors, such as antigen loss or modulation of the tumor microenvironment, can further hinder the efficacy of these therapies. Given these complications, having better *in vivo* imaging tools is essential for real-time monitoring of therapy dynamics, enabling researchers to track the distribution, activity, and potential adverse effects of engineered cells, thereby optimizing treatment strategies and improving patient outcomes.

Currently, clinical monitoring of these therapies primarily relies on biopsies or PET imaging[14]. While allowing for analysis of tissue samples, biopsies are invasive, not representative of the entire tumor, and inapplicable to tracking real-time changes. PET imaging, although valuable for assessing overall therapy distribution and metabolic activity, lacks the resolution needed to monitor cellular-level interactions and the finer details of therapy dynamics. Other techniques used in pre-clinical settings, such as bioluminescence imaging, suffer from the poor penetration depth of light. This underscores the need for a non-invasive, spatially scalable imaging technique with high resolution to monitor cell-based therapies once they are administered *in vivo*.

In Chapter 2, we address this gap by developing lentiviral vectors to deliver GV genes to T cells isolated from human peripheral blood mononuclear cells (PBMCs). This approach could enable longitudinal imaging of cell-based therapies in pre-clinical models, and should be applicable to other therapies such as stem cell-based ones. Ultimately, we hope this work will help make monitoring immunotherapies more accessible in clinical settings.

1.4 Non-invasive imaging of neural activity

Another area where there is a significant need for non-invasive imaging modalities is in the study of neural function on a brain-wide scale in large animals. Optical imaging techniques have made substantial progress, with fiber optometry enabling the imaging of neural activity in deep brain regions, and functional MRI (fMRI) allowing for the monitoring of neural activity across the entire brain. However, optical imaging, while capable of single-cell resolution, is limited in its application to studying brain function at a systems level. On the other hand, while fMRI can capture brain-wide activity, its resolution is several orders of magnitude lower than optical imaging, and there are currently no established reporter genes that can provide real-time monitoring of cellular function in the same way that GCaMP or transcriptional reporter genes do.

Ultrasound offers a promising alternative, achieving a resolution of approximately 100 μm, sufficient to image small clusters of cells[15]. One significant advancement in ultrasound technology is functional ultrasound imaging (fUSi), which enables the measurement of neural activity by measuring changes in blood flow associated with neuronal activation. Furthermore, with ongoing advancements in super-resolution techniques, it is anticipated that single-cell resolution may become achievable using ultrasound in the future. This positions ultrasound as a unique tool for studying neural function with higher resolution than current non-invasive imaging methods.

In Chapter 3, we present the development of a tool for delivering the GV gene cluster directly into the brain using a combination of three AAV vectors. We demonstrate how this tool can be used to track neural activity through immediate early gene (IEG)-induced expression of GVs, providing a novel approach to non-invasive monitoring of neural function at the systems level.

1.5 References

1. Maresca, D. *et al.* Biomolecular Ultrasound and Sonogenetics. *Annual Review of Chemical and Biomolecular Engineering* **9**, 229–252 (2018).
2. Christensen-Jeffries, K. *et al.* Super-resolution ultrasound imaging. *Ultrasound Med Biol* **46**, 865–891 (2020).
3. Shapiro, M. G. *et al.* Biogenic gas nanostructures as ultrasonic molecular reporters. *Nature Nanotech* **9**, 311–316 (2014).
4. Bourdeau, R. W. *et al.* Acoustic reporter genes for noninvasive imaging of microorganisms in mammalian hosts. *Nature* **553**, 86–90 (2018).
5. Hurt, R. C. *et al.* Genomically mined acoustic reporter genes for real-time in vivo monitoring of tumors and tumor-homing bacteria. *Nat Biotechnol* **41**, 919–931 (2023).
6. Buss, M. T., Zhu, L., Kwon, J. H., Tabor, J. J. & Shapiro, M. G. Probiotic acoustic biosensors for noninvasive imaging of gut inflammation. 2024.09.23.614598 Preprint at https://doi.org/10.1101/2024.09.23.614598 (2024).
7. Bar-Zion, A. *et al.* Acoustically triggered mechanotherapy using genetically encoded gas vesicles. *Nat. Nanotechnol.* **16**, 1403–1412 (2021).
8. Wu, D. *et al.* Biomolecular actuators for genetically selective acoustic manipulation of cells. *Science Advances* **9**, eadd9186 (2023).
9. Sawyer, D. P. *et al.* Ultrasensitive ultrasound imaging of gene expression with signal unmixing. *Nat Methods* **18**, 945–952 (2021).
10. Maresca, D., Sawyer, D. P., Renaud, G., Lee-Gosselin, A. & Shapiro, M. G. Nonlinear X-Wave Ultrasound Imaging of Acoustic Biomolecules. *Phys. Rev. X* **8**, 041002 (2018).
11. Farhadi, A., Ho, G. H., Sawyer, D. P., Bourdeau, R. W. & Shapiro, M. G. Ultrasound imaging of gene expression in mammalian cells. *Science* **365**, 1469–1475 (2019).
12. Hurt, R. C. *et al.* Directed Evolution of Acoustic Reporter Genes Using High-Throughput Acoustic Screening. *ACS Synth. Biol.* **13**, 2215–2226 (2024).
13. Duan, M. *et al.* SEMPER: Stoichiometric expression of mRNA polycistrons by eukaryotic ribosomes for compact, ratio-tunable multi-gene expression. *cels* **15**, 597-609.e4 (2024).
14. Volpe, A., Adusumilli, P. S., Schöder, H. & Ponomarev, V. Imaging cellular immunotherapies and immune cell biomarkers: from preclinical studies to patients. *J Immunother Cancer* **10**, e004902 (2022).
15. Rabut, C. *et al.* Ultrasound Technologies for Imaging and Modulating Neural Activity. *Neuron* **108**, 93–110 (2020).

Chapter 2

NON-INVASIVE IMAGING OF CELL-BASED THERAPIES USING ACOUSTIC REPORTER GENES

Shivaei, S., Liu, A., Abedi, M.H., Revilla, J., Hurvitz, I.U., Swift, M.B. and Shapiro, M.G.. Non-invasive imaging of cell-based therapies using acoustic reporter genes. *bioRxiv*, pp.2024-11 (2025). DOI: https://doi.org/10.1101/2024.11.01.621111

2.1 Introduction

Cell-based therapies are making breakthrough progress in treating complex diseases such as cancer and autoimmune disease. However, predicting and monitoring their *in vivo* dynamics, including tissue infiltration, proliferation, and off-target activity, remain challenging and necessitate the development of more advanced *in vivo* imaging methods. Existing imaging techniques used in research, such as luminescent reporters[1], provide poor spatial resolution due to light scattering, while clinical probes based on positron emission tomography require expensive radioligand synthesis and imaging equipment, and expose patients to radiation[2–6]. Improved imaging techniques are essential for understanding the mechanisms of cell-based therapies, optimizing treatment protocols, and ensuring precise targeting of therapeutic cells to improve their efficacy and reduce off-target effects, ultimately accelerating the development of new cell-based treatments.

Ultrasound presents a promising modality to track cell therapies, as it is affordable, widely available in medical settings, and capable of large-scale scanning of deep organs with spatial resolution on the order of 100 micrometers[7]. To enable *in vivo* imaging of cell therapies with ultrasound, one would ideally use reporter genes rather than synthetic labels, as this would allow the tracking of proliferating cells without signal dilution and the sensing of specific cellular states via promoter-driven expression.

Here we introduce a method to track cell therapies with ultrasound using acoustic reporter genes based on gas vesicles (GVs). GVs are microbially derived air-filled protein nanostructures that scatter sound waves, enabling their use as reporter genes for ultrasound imaging in mammalian cells[8–10] and probiotics[11,12,9,13]. However, previous mammalian uses of GVs have been limited to chemical transfections of the GV gene cluster, restricting their use to transfection-compatible

cell lines. In fact, to date there has been no demonstration of GV gene expression in primary cells due to the difficulty of delivering the eight or more genes encoding GVs, at appropriate stoichiometries, to such cells using compatible methods such as viral delivery.

To overcome this challenge, we designed, optimized and extensively characterized a lentiviral vector architecture capable of delivering the complete set of GV-encoding genes into mammalian cells, resulting in robust ultrasound contrast. We showed that GV expression can be driven by a chemically inducible promoter or connected to a gene circuit engineered to respond to cell activity, permitting the imaging of receptor-driven immune cell activation. We used our lentiviral expression system to produce GV-expressing primary human T cells and used ultrasound to monitor their accumulation *in vivo* as an adoptively transferred cell therapy in mouse tumor xenografts, as corroborated by immunohistochemistry. These results position virally-encoded GVs as a prime option for ultrasound imaging of cell-based therapies.

2.2 Results

2.2a Optimized lentiviral vector design enhances GV gene cluster delivery and expression in mammalian cells.

To enable their use as acoustic reporters in primary cells, we sought to package the genes encoding GVs into lentiviral vectors — the most established delivery vehicle in clinical cell engineering[14]. Lentiviral packaging and transduction efficiency depend heavily on transgene size, with a packaging limit of 8-10 kilobases (kb) and reduced titers with larger payloads in this range[15]. The smallest GV gene cluster expressed in mammalian cells, derived from *Anabaena flos-aquae*, comprises 8 genes, which take up 4.5 kb without promoters and other genetic elements required for polycistronic expression[9]. To establish a strategy for efficient lentiviral GV expression, we decided to compare three vector architectures in which the genes are combined across one, two, or three co-transduced viral constructs. We then transduced HEK293T cells with each viral combination at different multiplicities of infection (MOIs) and measured the ultrasound contrast of the cells embedded in hydrogel phantoms (**Fig. 2-1a**). We used two nonlinear ultrasound imaging methods optimized for GV detection, BURST[16] and xAM[17]. The former makes use of the strong nonlinear scattering produced immediately after collapsing GVs with a high-pressure pulse, while the latter non-destructively captures nonlinear scattering arising from reversible buckling of the GVs with each cycle of the transmitted sound wave.

In our first design, we used a single lentiviral backbone to encode the main structural protein *gvpA* and all seven GV assembly factor genes (*gvpN-V*), along with a fluorescent marker (GFP), under a TRE promoter (**Fig. 1b**). This promoter, used in conjunction with an rtTA transactivator, drives expression in the presence of doxycycline, allowing GV production to be timed with imaging to minimize metabolic burden. We linked *gvpA* to the assembly factors (AFs) via an internal ribosome entry site (IRES), while the AF genes were themselves polycistronically linked using self-cleaving 2A peptides (iterating through P2A, T2A, E2A, and F2A, to minimize the risk of homology-induced genetic recombination). The total packaging size was 8.8 kb. We transduced a HEK-TetON cell line with this virus, while varying the MOI from 1 to 15. We observed BURST ultrasound contrast at all MOIs, with the strongest signal at MOIs of 1, 5, and 10 and decreasing at MOI of 15 (**Fig. 2-1c, d**). The xAM contrast was strongest at MOI of 5 and decreased at MOIs of 10 and 15 (**Fig. 2-S1a**). The highest MOIs also showed reduced infectivity via flow cytometry, suggesting toxicity from high viral burden (**Fig. 2-2Sa, b**). These results show that it is possible to express GVs in mammalian cells using viral vectors, and that the entire GV gene cluster can fit into a single lentiviral construct. While recognizing these important milestones, we hypothesized that breaking the construct up into two or three smaller inserts would allow more efficient viral packaging and transduction, provide flexibility to control gene stoichiometry, and make room to include the rtTA transactivator to enable expression in previously unengineered cells.

Thus, our second design comprised two vectors: one encoding the main structural protein *gvpA* and rtTA, and the second encoding all the AFs, *gvpN-V* (**Fig. 2-1e**). These vector inserts had lengths of 5.1 and 8 kb, respectively. This two-vector design enabled us to adjust the copy number of *gvpA* relative to the AFs, a variable shown to impact GV expression in mammalian cells[9]. Transducing a HEK293T cell line, we maintained a total MOI of 10 while varying the MOI ratio between the *gvpA* and the AF vectors. We found that all ratios produced significant ultrasound contrast in BURST (**Fig. 1f-g**) and xAM (**Fig. 2-S1b**), peaking at 2:1 and 4:1 ratios, respectively. Transduction was similar across all ratios, remaining above 40%, and the expression of BFP and GFP followed the ratios of the *gvpA* and AF vectors as expected (**Fig. 2-S2c, d**).

In our third design, we split the seven AF genes across two vectors, grouping *gvpNJKF* (AF1) and *gvpGWV* (AF2), respectively, with packaging sizes of 6.7 and 4.8 kb. We encoded *gvpA* on its own third virus with an insert length of 4 kb (**Fig. 2-1h**). The rtTA was included on the AF1

construct. Using a constant total MOI of 10 while testing three ratios of the *gvpA* vector relative to the two AF vectors, we observed much stronger BURST contrast compared to the one- and two-vector designs (**Fig. 2-1i, j**), with the highest signal-to-background ratio (SBR) at the 4:1:1 ratio, measured to be 118 ± 8.4 (mean ± s.e.m.). The xAM signal was similarly improved and increased with more *gvpA* (**Fig. 2-S1c**). Transduction efficiency was comparable to the 2-vector design (**Fig. 2-S2e, f**). Cell viability was not affected by viral transduction or the induction of GV expression (**Fig. 2-S2g**). These results demonstrate that a split-vector approach comprising smaller inserts and more flexibility in ratiometric expression provides the best performance for expressing the polycistronic GV complex.

Using our best-performing three-vector transduction system (4:1:1), we quantified ultrasound contrast as a function of cell concentration after sorting for triple-transduced cells. Significant signal from the cells could be detected at a concentration of 1e6 cells per milliliter with BURST (**Fig. 2-1k**) and with xAM (**Fig. 2-1l**). This concentration corresponds to approximately 4 cells per image voxel (where each voxel is 0.004 mm^3) and a volume fraction of approximately 0.9%. Thus, we concluded that viral vector delivery enables highly sensitive imaging of GV-expressing cells and adopted the three-vector design for the rest of our experiments.

2.2b Lentiviral GV delivery system is adaptable for robust transduction and ultrasound imaging of immune cells.

We next asked if our lentiviral GV delivery architecture could be adapted to image immune cells, starting with the Jurkat T cell line, which is commonly used to model lymphocyte-based cell therapies (**Fig. 2-2a**). Since Jurkats are more difficult to transduce than HEK239T cells[18], we hypothesized that they would require higher viral doses to achieve similar levels of transduction. We therefore incubated the Jurkat cells with total MOIs of 30 and 60 (as defined based on functional tittering in HEK cells), varying the *gvpA*-to-AF1 and AF2 ratio within each MOI. While both MOIs resulted in appreciable ultrasound signal at certain ratios, the most consistent BURST contrast was produced at MOI of 60, with the 4:1:1 ratio showing the highest BURST SBR at 5.94 ± 1.64 (**Fig. 2-2b, c**), and the strongest signal in xAM (**Fig. 2-S3a, b**). As expected, cells transduced with the higher MOI had a larger number of triple-transduced cells (**Fig. 2-S4a**) and higher levels of GFP and BFP expression (**Fig. 2-S4b, c**).

Triply transduced and sorted cells in the MOI 60 - 4:1:1 condition showed significant BURST contrast at concentrations as low as 1e6 cells per milliliter (**Fig. 2-2d**). xAM was able to detect as few as 1e7 cells per milliliter (**Fig. 2-2e**).

We measured the viability of Jurkat cell lines transduced with the 3-vector system, with and without inducing GV expression. Using 7-AAD (7-aminoactinomycin D) live/dead staining, we found no significant doxycycline-induced cell death attributed to GV expression (**Fig. 2-S4d, e**). However, we saw overall more cell death in cells transduced with the three vectors at MOI 60 compared to MOI 30. We attribute this to the high viral dose, which likely included a large number of empty capsids from packaging larger payloads[19].

These experiments together demonstrated the adaptability of our lentiviral architecture for expressing GVs in immune cells, and more generally, in cells considered to be more difficult to transduce.

2.2c Acoustic reporter genes enable monitoring of T cell activation.

Having engineered immune cells to express GVs, we hypothesized that this expression could be connected to an activity-dependent promoter as a read-out of cellular state. In particular, we sought to trigger ultrasound contrast in T cells when they become activated by antigen engagement. To achieve this goal, we connected GV expression to the NFAT promoter, which activates upon T cell receptor engagement and accompanying calcium influx[20,21]. We constructed a gene circuit in which the NFAT promoter is placed upstream of the rtTA transactivator, such that NFAT activation initiates transcription of the rtTA, which in the presence of doxycycline drives GV gene transcription (**Fig. 2-3a**). This architecture is beneficial because it allows potentially weak NFAT activity to drive a stronger rtTA-TRE transcription complex and temporally confines GV expression to periods when it is needed for imaging, thereby minimizing cellular burden. This architecture is also modular in the sense that only a simple swap of the promoter upstream of rtTA is needed to change the conditionality of expression for all eight GV genes and accompanying fluorophores.

We created a Jurkat T cell line transduced with this engineered three-virus combination and tested whether we can turn on GV expression by chemically inducing the NFAT promoter. When we stimulated these cells with phorbol 12-myristate 13-acetate (PMA) and ionomycin[22] in the presence of doxycycline, they produced strong ultrasound contrast (**Fig. 2-3b**). The signal was activity-specific, with a fold-change of 10.9 in BURST SBR when compared with

doxycycline alone. Flow cytometry confirmed specific circuit activation, with an activation-dependent fold change of 99.0 in the fraction of cells expressing GFP and BFP (**Fig. 2-3c**).

Having confirmed the circuit design, we tested if receptor-induced activity could be detected with ultrasound when T cells engage with an on-target bait cell. We used a CD19-CD3 bispecific T-cell engager (BTE), which causes T cell activation when a BTE molecule binds CD3 on the T cell surface and CD19 on the target cell surface at the same time[23]. We co-cultured our NFAT-inducible Jurkat cell line with CD19+ Raji cells at a 1:1 ratio (**Fig. 2-3d**). Within 24 hours, in the presence of the BTE, we observed a large increase of ultrasound contrast (4.8-fold change in BURST SBR) relative to the same co-culture without the molecular engager (**Fig. 2-3e**). Flow cytometry corroborated this activation by showing a 22.1-fold change in the GFP and BFP positive population fraction (**Fig. 2-3f**). These results highlight the potential of ultrasound to detect cellular activation states by leveraging activity-dependent transcription to drive GV expression.

2.2d Ultrasound monitors in vivo homing of GV-expressing therapeutic T cells into tumors.

A major challenge in cell-based therapies is to monitor the trafficking of engineered cells to their intended target tissues after *in vivo* administration. To address this challenge, we endeavored to show that we could use our viral GV expression platform to label a primary T cell therapy and image its homing to tumors following systemic infusion.

To achieve this goal, we isolated primary T cells from human peripheral blood mononuclear cells (PBMCs) and transduced them with our doxycycline-dependent 3-vector system. Since at a total viral titer of MOI 120 (based on functional tittering in HEK cells), less than 20% of these hard-to-transduce cells[24,25] were triple-positive for all three viruses, we used a 1:1:1 ratio of the *gvpA* to AF1 and AF2 vectors to maximize the number of cells with at least one functional unit of each construct (**Fig. 2-4a**, top row). After sorting the cells based on GFP expression to ensure that they received all assembly factor genes, and inducing them with doxycycline for 72 hours, we found a consistent BURST signal in doxycycline-induced T cells of five different human donors that was 3.8 ± 0.2 times (geometric mean of ratios ± s.e.m. of log(ratios)) higher than the signal from wild-type non-transduced cells (**Fig. 2-4b**), marking the first demonstration of primary mammalian cells expressing acoustic reporter genes. Of the doxycycline-induced sorted cells, 55.8 ± 7.36% (N = 5, mean ± s.e.m) were both GFP and BFP positive, indicating the presence of both AFs and *gvpA* in most of this population (**Fig. 2-S5**).

After demonstrating ultrasound contrast, we asked if GV expression affects T cell cytotoxicity, a critical function for administered therapies. To investigate this, we co-cultured the T cells with CD19+ Raji cells at 1:1 and 4:1 effector-to-target (E:T) ratios in the presence of the CD19-CD3 BTE, and measured the percentage of live target cells with 7-AAD staining 24 hours after co-culture. We found that GV expression (controlled with doxycycline induction) did not affect T cell cytotoxicity at either ratio, and as expected the cells were more effective at killing at the higher E:T ratio and in the presence of the targeting BTE (**Fig. 2-4c**). Interestingly, flow cytometry showed increased GFP and BFP expression in co-cultured T cells with BTE engagement, especially at the higher E:T ratio (**Fig. 2-4d**). This is because increasing the E:T ratio leads to more efficient target cell lysis, and hence increased T cell activity and protein expression[26–29].

Having demonstrated successful GV expression and ultrasound imaging *in vitro*, we designed an experiment to show that primary T cells could be imaged *in vivo* after systemic administration, allowing ultrasound to visualize their trafficking to tumors. We intravenously infused the engineered T cells into immunocompromised mice bearing subcutaneous CD19+ Raji cell flank tumors, followed by intraperitoneal (IP) injections of the CD19-CD3 BTE every 2 days to stimulate activation and local expansion inside the tumor microenvironment[23,30]. On day 3 after T cell infusion, we induced GV expression with intraperitoneal doxycycline and imaged the tumors with ultrasound (protocol depicted in **Fig. 2-4a**, bottom row).

Ultrasound imaging revealed clear BURST ultrasound contrast in the tumors of mice infused with GV-expressing T cells and induced with doxycycline (**Fig. 2-4e, f**). This signal was absent in mice that were not doxycycline-induced or received wild-type T cells. This response was consistent across our total cohort of 22 mice, with 4.1 fold-change in BURST SBR for the Dox+ vs. Dox- groups, and 4.3 for the Dox+ vs. WT groups (**Fig. 2-4f** and **Fig 2-S6**). In a subset of animals, we collected tumors and performed immunofluorescence imaging to confirm that the localization of ultrasound signal observed in tumors matches the spatial distribution of GV-expressing T cells observed by histology, finding a clear correspondence (**Fig. 2-4g** and **Fig. 2-S7**). For example, in a representative tumor, the core was mostly necrotic with few live cells, while both ultrasound and histology showed cytotoxic T cells expressing our reporter construct concentrated at the viable tumor periphery near the top of the tumor (**Fig. 2-4g, h**). The ability of ultrasound to visualize this sub-tumor localization *in vivo* is in stark contrast to the diffuse signal typically obtained with bioluminescence or nuclear imaging methods.

Notably, tumors with low ultrasound contrast also had few T cells by histology (**Fig. 2-S7**). Indeed, we found a strong positive correlation between the absolute number of GFP+ and BFP+ T cells counted in a given histology slice *postmortem* and the BURST signal measured in the corresponding ultrasound image plane *in vivo* ($r = 0.89$, $p = 0.0072$, Pearson correlation, **Fig 2-4i**), suggesting that ultrasound can provide a quantitative noninvasive readout of cell therapy homing and/or expansion.

Overall, these experiments demonstrated, for the first time, an ultrasound method to noninvasively visualize the homing of a mammalian cell therapy into its target tissue.

2.3 Discussion

This work introduces a genetic technology platform enabling the use of acoustic reporter genes to image a broader variety of cell types, including primary cells deployed in an *in vivo* cell therapy context. By devising a set of suitable viral constructs, we make it possible to introduce GV genes into transfection-resistant cells such as T cells, with our most effective system comprising a combination of three lentiviral vectors encoding the 8 essential GV genes, along with an rtTA transactivator and fluorescent proteins for correlative histology. In addition, we showed how this expression system can be easily modified to monitor cellular states using activity-dependent promoters. Furthermore, we demonstrated that this system enables the noninvasive *in vivo* monitoring of therapeutic T cell homing and proliferation in tumors with a combination of penetration depth and resolution not available with other modalities.

This acoustic imaging toolkit will significantly advance preclinical studies by allowing the study of the dynamics of cell-based therapies *in vivo*, such as how adoptively transferred T cells infiltrate solid tumors and where they expand within the tumor microenvironment. Additionally, it could facilitate the monitoring of off-tumor on-target cytotoxicity, a common side effect of CAR T cells by imaging bystander organs. More broadly, our approach opens new possibilities to study the *in vivo* dynamics of other cell-based therapies, including those based on natural killer (NK) cells, macrophages, stem cells, and any other cell types that can be engineered with viruses, and to track cellular states beyond T cell activation, such as during different stages of development. Beyond preclinical research, we envision the use of something like these acoustic reporter gene constructs in future clinical applications, allowing physicians to check that the therapy they administer reaches the right tissues and performs their intended activities. Such applications would take advantage of the ubiquitous accessibility of ultrasound imaging devices

and the emergence of new form factors such as continuously wearable bio-adhesive ultrasound patches[31–34].

As expected for the first demonstration of a new imaging approach, our toolkit can benefit from further improvements. The high MOI required for efficient co-transduction of multiple vectors in primary T cells[35] could be burdensome for certain cells and expensive to manufacture at scale. We anticipate that this limitation will be overcome with future improvements in GV expression efficiency through modified assembly factor stoichiometry[10] or mutagenesis of the GV genes themselves[36]. Further gains could be made by optimizing the expression cassette with improved cell type-specific promoters, targeted genomic integration and addition of elements to reduce epigenetic silencing[37]. Another limitation is that our primary T cells were detectable only with collapse-based BURST imaging, which, while highly sensitive, requires re-expression of GVs for repeated imaging. This is likely because the GVs formed in primary T cells are too small to undergo the reversible mechanical buckling needed for non-destructive xAM imaging[38,39]. This issue would also be addressed with further gene and protein engineering for more efficient expression. Additionally, using more advanced ultrasound hardware, such as matrix or row-column arrays, could improve the sensitivity and fidelity of xAM[40] and BURST imaging by generating a more homogeneous pressure field within the target tissue and minimizing the potential for motion artifacts.

Using the technology developed in this study, ultrasound can now be utilized to image primary mammalian cells, including therapeutic cells, *in vivo*. With further improvements, getting a quick ultrasound may become as common for checking on a cell therapy as it is for checking on a growing fetus.

2.4 Methods

Plasmid construction and molecular biology

All constructs were made via KLD mutagenesis or Gibson Assembly using enzymes from New England BioLabs. All plasmids and their sources of genetic material are described in Supplementary Table 1. Constructs were cloned in NEB Turbo Competent E. coli (High Efficiency, Catalog #C2984). Fluorescent reporters referred to in the text as GFP and BFP are mEGFP and mTagBFP2, respectively.

Lentivirus packaging, titrating, and transduction

Packaging: DMEM+ media for packaging was prepared by supplementing high-glucose DMEM + GlutaMAX containing 1 mM sodium pyruvate (Gibco, Catalog #10569), with 20 mM HEPES (Cytvia, Catalog #SH30237**)**, 1X MEM-Non-Essential Amino Acids (0.1 mM, Gibco #11140), and 10% fetal bovine serum (bio-techne, Catalog # S10350). HEK293T cells (ATCC, CRL-3216), passaged no more than 20 times, were seeded in 10 cm plates and grown in DMEM+ until they reached 80 - 90% confluence. A mixture of 22 µg pLV (plasmid with the gene of interest), 22 µg pCMVR8.74, and 4.5 µg pMD2.G was prepared. These plasmids were combined with polyethylenimine (PEI Max, Polysciences) at a PEI to DNA mass ratio of 3:1, incubated at room temperature for 12 minutes, and then added to the cells. Cells were incubated at 37°C and 5% CO2 for 12 hours. After this period, the transfection media was replaced with 10 mL of fresh DMEM+. After 48 hours, the spent media was collected and centrifuged at 500g for 10 minutes to remove debris. The viral supernatant was then concentrated 100-fold into 1X phosphate-buffered saline (PBS) using LentiX Concentrator (Takara Bio, Catalog #631232), following the manufacturer's protocol. The concentrated virus was aliquoted and stored at -80°C for up to 6 months, avoiding freeze-thaw cycles.

Measuring titer: For the NFAT-inducible virus, LentiX GoStix Plus (Takara Bio, Catalog #631281) was used to measure the titer, following manufacturer's instructions. All other viruses were functionally titrated in various HEK-based cell lines, as described below, following the protocol outlined here. Cells were seeded in 24-well plates in DMEM and grown to 70 - 90% confluence. Three wells were trypsinized, and the average of their cell count was used in calculating the titer, described below. A serial dilution of the virus was prepared in fresh DMEM and added to each well. Plates were spun for 50 minutes at 800g at 35°C and then incubated at 37°C and 5% CO2 for 16-20 hours. The media was aspirated and replaced with fresh DMEM, supplemented with doxycycline (1 µg/mL) for the HEK-TetON and HEK-TRE cell lines. Cells were incubated for an additional 24 hours before being prepared for flow cytometry. Gating strategy for flow cytometry is shown in **Supplementary Fig. 2**. The functional titer of each virus was calculated using the following formula:

$$TU/mL = \frac{average\ cell\ count\ (on\ day\ of\ infection) \times \%\ fluorescence}{viral\ volume}$$

Only dilutions resulting in less than 30% fluorescent cells were used for the calculation. This threshold was chosen because it ensures that the probability of any cell receiving more than one functional viral particle is less than 26%.

The following HEK293T-based cell lines were used for functional titering: 1) wild-type HEK293T cells used to titrate any virus expressing a fluorescent protein constitutively, 2) HEK-TetON cells used to titrate any virus expressing a fluorescent protein downstream of the TRE promoter, 3) HEK-TRE cells engineered to express mScarlet-I downstream of TRE, and used to titrate any virus expressing rtTA.

Transduction: To transduce HEK293T cells, the cells were seeded in 12-well plates 24 hours before transduction and grown to 70 - 90% confluence. On the day of transduction, cells from three wells were counted and averaged to determine the viral volume needed for each desired MOI. Lentivirus was mixed with fresh media and added to each well with 10 μg/mL of polybrene (Millipore Sigma, Catalog #TR1003). Cell culture plates were spun at 800g for 50 minutes at 35°C, and incubated at 37°C for 16-20 hours. The viral media was then removed, and the cells were passaged for downstream applications.

To transduce suspension cells (Jurkats and primary T cells), the cells were counted on the day of transduction and one million cells were mixed with fresh media and virus at the desired MOI. The cells were spun at 1000g for 50 minutes at 35°C, then incubated at 37°C for 16-20 hours. Viral media was then removed, and the cells were passaged for further use.

Cell Viability

All cell viability experiments were performed using the 7-AAD viability stain (BioLegend, Catalog #420403) according to the manufacturer's protocol. Briefly, the cell pellet was resuspended in 100-200 μL of 1X PBS, and 7-AAD stain was added at a 1:100 dilution. Cells were incubated for 5-10 minutes in the dark, and flow cytometry measurements were taken immediately afterward using the MacsQuant Analyzer 10.

Cell sorting

Cells were expanded without prior doxycycline addition and induced for the first time with doxycycline (1 μg/mL) 24 hours before sorting. Cells were collected and resuspended in cell sorting buffer (Miltenyi Biotec, Catalog #130-107-207) at a concentration of 2-4 million cells/mL, and GFP- and BFP-expressing cells were sorted using the MACSQuant Tyto cell sorter. For primary T cells, doxycycline induction (1 μg/mL) was done for 48 hours, followed by resuspension in RPMI media without FBS, and sorting based on GFP expression. Sorted cells

were immediately resuspended in their respective media and incubated at 37°C, with a recovery period of at least 24 hours before use in downstream experiments.

In vitro T cell activity induction

For chemical induction, Jurkat cells (Clone E6-1, ATCC #TIB-152) were stimulated with 50 ng/mL phorbol 12-myristate 13-acetate (VWR, Catalog #16561-29-8) and 1.3 µM ionomycin (Sigma, Catalog #I9657) for 24 hours before being used for flow cytometry (MacsQuant Analyzer 10) and ultrasound imaging. For receptor-mediated induction, Jurkat cells were co-cultured with Raji cells (ATCC, CCL-86) at a 1:1 ratio in media supplemented with 1 ng/mL CD19-CD3 BTE (BPS Bioscience, Catalog #100441). Similar to chemical induction experiments, cells were used for flow cytometry and ultrasound imaging after 24 hours of co-culture.

T cell isolation, transduction, and sorting

T cells were isolated from frozen human peripheral blood mononuclear cells (STEMCELL, Catalog #70025.1) using the EasySep Human T Cell Isolation Kit (STEMCELL, Catalog #17951), and activated with Dynabeads Human T-Activator CD3/CD28 beads (Gibco, Catalog #1131D). T cells were cultured in RPMI supplemented with GlutaMAX (Gibco, Catalog #61870036) and recombinant human IL-2 at 100 U/mL (Miltenyi Biotec, Catalog #130-097-743). 16-20 hours after isolation/activation, the cells were transduced with lentivirus as described above. Media containing virus was removed 16-20 hours after transduction. The cells were passaged every other day to maintain a density of 1e6 cells/mL, and provided with IL-2 at 100 U/mL. Activation beads were removed on day 5 post-isolation/activation. Fluorescence was induced with doxycycline for 2 days, and GFP-positive cells were sorted using the MACSQuant Tyto Cell Sorter (Miltenyi Biotec) on day 7. The sorted cells were then expanded *in vitro* for further use.

Cell preparation and phantom loading for in vitro imaging

Adherent cells were seeded 24 hours in advance and allowed to reach 70 - 80% confluence. They were then induced with doxycycline hyclate at 1 µg/mL every 24 hours for 72 hours. On the day of imaging, cells were trypsinized, spun down at 300g for 5 minutes, and resuspended in 1X PBS. They were briefly mixed with 1% melted agarose in 1X PBS (1:1 dilution at 42°C)

and loaded into agarose phantoms at a final concentration of 25 million cells/mL for all experiments, except detection limit experiments.

Suspension cells were resuspended to 0.8e6 cells/mL on the day of induction, and supplemented with doxycycline at 1 μg/mL every 24 hours for 72 hours. Meanwhile the cells were passaged to keep their density below 1e6 cells/mL. On the day of imaging, cells were spun down at 300g for 5 minutes and resuspended in 1X PBS. They were briefly mixed with 1% melted agarose in 1X PBS (1:1 dilution at 42°C) and loaded into agarose phantoms at a final concentration of 25 million cells/mL for all experiments, except detection limit experiments. Primary T cells were loaded at 50 million cells/mL.

In vitro killing assay

Primary T cells were mixed with Raji cells to achieve a final density of 1 million cells/mL. To induce receptor-mediated T cell cytotoxicity, CD19-CD3 BTE (1 ng/mL, BPS Bioscience, #100441) and IL-2 (100 U/mL) were added. After 24 hours of co-culture, the percentage of live Raji cells was measured using 7-AAD (BioLegend, Catalog #420403) staining with flow cytometry, following the manufacturer's protocol.

Tumor implantation and T cell injections in mice

NSG mice (NOD-scid IL2Rgamma, JAX, Strain #005557) aged 3 to 8 months were used. 4 million Raji cells expressing the Antares fluorescence reporter[41] under the Ef1a promoter were resuspended in matrigel (Corning, Catalog # 354234) on ice and injected subcutaneously near the flank. When tumors reached a measurable size between days 12 to 17 after implantation, the mice were infused with 10 million T cells via tail-vein injections. BTE (0.25 mg/kg in saline, BPS Bioscience, #100441) and doxycycline hyclate (4 mg/kg, in saline) were administered intraperitoneally according to the timeline in **Fig. 4a,** with the first BTE dose administered 30 min before T cell injection. Hair around the tumor was shaved immediately before imaging, and mice were anesthetized under 1-2.5% isoflurane during imaging.

Immunohistochemistry of tumors

Tumors were extracted from mice following ultrasound imaging and fixed overnight in 4% paraformaldehyde at 4°C with continuous rotation. They were then immersed in 30% sucrose for 48 hours before embedding in O.C.T. Compound (Fisher Scientific, Catalog #23-730-571) at -80°C. The frozen tissue was cryosectioned at a thickness of 20 μm, with 3 to 6 slices collected

every 1 mm and placed directly onto microscope slides (Fisher Scientific, Catalog #12-550-19). The location of each cryosectioned slice was recorded to match it to the corresponding BURST plane with 1 mm accuracy. Slides were dried overnight at room temperature and stored at -80°C.

Before staining, slides were brought to room temperature and washed in 1X PBS for 5 minutes, repeated three times. They were then incubated in freshly prepared blocking buffer (5% bovine serum albumin in 1X PBS) for 60 minutes at room temperature. After blocking, slides were washed in 1X PBS for 5 minutes, repeated twice. Most of the PBS was then removed, and a liquid blocker pen (Ted Pella, Catalog #22311) was used to draw boundaries around tumor slices on each slide. The antibody dilution was prepared in freshly made staining buffer (0.5% bovine serum albumin in 1X PBS). To each slide, 200 µL of the antibody solution was added, ensuring it covered all tumor slices, and slides were incubated overnight at 4°C in a humid chamber. The slides were washed in 1X PBS for 5 minutes, repeated three times, and excess PBS was removed.

Next, 200 µL of mounting media (Electron Microscopy Sciences, Catalog #17985-11) was added to each slide, which was then sealed with a coverslip. Slides were allowed to dry before imaging and protected from light throughout all staining steps. The following antibody was used for staining CD8+ T cells: Alexa Fluor 647-conjugated anti-human CD8 antibody (BioLegend, Catalog #344726) at a 1:50 dilution.

Confocal imaging was performed using an inverted laser scanning confocal microscope with a 20x objective lens. Cell counting was conducted using the Imaris software's Spots Detection function based on GFP and BFP expression. Briefly, images were initially processed with a Gaussian blurring filter. The Spots Detection function was applied separately to the GFP and BFP channels to mark fluorescent cells. The number of overlapping GFP+ and BFP+ spots inside the tumor were then counted.

Ultrasound data acquisition and image analysis

In vitro imaging: Ultrasound imaging for *in vitro* experiments was performed using a Verasonics Vantage programmable ultrasound scanning system with an L22-14vX 128-element linear array transducer (Verasonics). Image acquisition was conducted using previously published BURST and xAM scripts. For BURST imaging, the transmit waveform was set to a frequency of 15.6 MHz, with a 67% intra-pulse duty cycle, and 7 half-cycle transmits. The BURST pulse sequence consisted of a single low-pressure frame (transducer voltage: 1.6 V; peak positive pressure: 0.4 MPa) followed by forty-five high-pressure frames (transducer voltage: 15 V; peak positive

pressure: 3.6 MPa). The programmable transmit focus was set to 8 mm to align with the fixed elevation focus of the transducer.

All *in vitro* BURST images were reconstructed using a temporal-template unmixing algorithm across individual pixel locations in the frame stack[16]. Signal-to-background ratio (SBR) was defined as the mean BURST signal within an ROI drawn inside the well, divided by the mean BURST signal in WT/non-transduced wells for each experiment.

For xAM imaging, cells were imaged over a range of pressures (peak positive pressure 0.2 MPa to 1.1 MPa; transducer voltage 3.5 V to 9.5 V). The pressure yielding the highest signal-to-noise ratio before GV collapse was selected for quantification. xAM SBR was defined as the mean xAM signal within an ROI drawn inside the well, divided by the mean signal in a noise ROI drawn in the phantom adjacent to the well.

In vivo imaging: The same Verasonics Vantage system and transducer were used in both *in vitro* and *in vivo* experiments. The BURST pulse sequence began with a single low-pressure frame (transducer voltage: 1.6 V), followed by five high-pressure frames (transducer voltage: 25 V). Multiple transmit foci were employed to capture the entire tumor, with a BURST image acquired at each focus. These images were summed to create a composite BURST image. Each cross section of tumor was imaged twice, with the second acquisition used for background normalization (details below).

BURST images were reconstructed by subtracting the 5th post-collapse frame from the collapse frame to isolate collapse-based nonlinear scattering from linear scatterers. Images with different transmit foci were then summed to create a composite image, which was subsequently processed with a Gaussian blur filter ($\sigma = 0.5$). The region of interest (ROI) was defined as the entire region within the tumor, excluding any contrast outside this ROI from analysis. The normalized signal-to-background ratio (SBR) was calculated by dividing the BURST signal within the ROI of the first acquisition by the signal within the same ROI of the second acquisition. The anticipated depth-dependent distribution of captured BURST signal is shown in **Fig. 2-S8**.

In all images, decibels (dB) was defined as following:

$$dB = 20 \times log_{10}(SBR)$$

Statistical Analysis

All statistical tests were performed with Prism 10 (Graphpad). All tests were performed with 95% confidence intervals. Standard deviations were checked to make sure appropriate t tests were performed. No other methods were used to determine if data satisfied the assumptions made in the statistical tests.

2.5 References

1. Santos, E. B. *et al.* Sensitive in vivo imaging of T cells utilizing a membrane bound Gaussia princeps luciferase enzyme. *Nat Med* **15**, 338–344 (2009).
2. Tavaré, R. *et al.* Engineered antibody fragments for immuno-PET imaging of endogenous CD8+ T cells in vivo. *Proceedings of the National Academy of Sciences* **111**, 1108–1113 (2014).
3. Mall, S. *et al.* Immuno-PET Imaging of Engineered Human T Cells in Tumors. *Cancer Research* **76**, 4113–4123 (2016).
4. Wei, W., Jiang, D., Ehlerding, E. B., Luo, Q. & Cai, W. Noninvasive PET Imaging of T cells. *Trends in Cancer* **4**, 359–373 (2018).
5. Ashmore-Harris, C., Iafrate, M., Saleem, A. & Fruhwirth, G. O. Non-invasive Reporter Gene Imaging of Cell Therapies, including T Cells and Stem Cells. *Molecular Therapy* **28**, 1392–1416 (2020).
6. Sellmyer, M. A. *et al.* Imaging CAR T Cell Trafficking with eDHFR as a PET Reporter Gene. *Molecular Therapy* **28**, 42–51 (2020).
7. Maresca, D. *et al.* Biomolecular Ultrasound and Sonogenetics. *Annual Review of Chemical and Biomolecular Engineering* **9**, 229–252 (2018).
8. Farhadi, A., Ho, G. H., Sawyer, D. P., Bourdeau, R. W. & Shapiro, M. G. Ultrasound imaging of gene expression in mammalian cells. *Science* **365**, 1469–1475 (2019).
9. Hurt, R. C. *et al.* Genomically mined acoustic reporter genes for real-time in vivo monitoring of tumors and tumor-homing bacteria. *Nat Biotechnol* **41**, 919–931 (2023).
10. Duan, M. *et al.* SEMPER: Stoichiometric expression of mRNA polycistrons by eukaryotic ribosomes for compact, ratio-tunable multi-gene expression. *cels* **15**, 597-609.e4 (2024).
11. Bourdeau, R. W. *et al.* Acoustic reporter genes for noninvasive imaging of microorganisms in mammalian hosts. *Nature* **553**, 86–90 (2018).
12. Bar-Zion, A. *et al.* Acoustically triggered mechanotherapy using genetically encoded gas vesicles. *Nat. Nanotechnol.* **16**, 1403–1412 (2021).
13. Buss, M. T., Zhu, L., Kwon, J. H., Tabor, J. J. & Shapiro, M. G. Probiotic acoustic biosensors for noninvasive imaging of gut inflammation. 2024.09.23.614598 Preprint at https://doi.org/10.1101/2024.09.23.614598 (2024).
14. Milone, M. C. & O'Doherty, U. Clinical use of lentiviral vectors. *Leukemia* **32**, 1529–1541 (2018).
15. Yacoub, N. al, Romanowska, M., Haritonova, N. & Foerster, J. Optimized production and concentration of lentiviral vectors containing large inserts. *The Journal of Gene Medicine* **9**, 579–584 (2007).
16. Sawyer, D. P. *et al.* Ultrasensitive ultrasound imaging of gene expression with signal unmixing. *Nat Methods* **18**, 945–952 (2021).
17. Maresca, D., Sawyer, D. P., Renaud, G., Lee-Gosselin, A. & Shapiro, M. G. Nonlinear X-Wave Ultrasound Imaging of Acoustic Biomolecules. *Phys. Rev. X* **8**, 041002 (2018).
18. Zhang, X. *et al.* The effect of lentivirus-mediated expression of tumor necrosis factor related apoptosis-inducing ligand and shRNA against Bcl-2 on the growth of lymphoma cells. *Leukemia & Lymphoma* **53**, 710–717 (2012).
19. Sweeney, N. P. & Vink, C. A. The impact of lentiviral vector genome size and producer cell genomic to gag-pol mRNA ratios on packaging efficiency and titre. *Mol Ther Methods Clin Dev* **21**, 574–584 (2021).
20. Hogan, P. G. Calcium–NFAT transcriptional signalling in T cell activation and T cell exhaustion. *Cell Calcium* **63**, 66–69 (2017).
21. Jutz, S. *et al.* Assessment of costimulation and coinhibition in a triple parameter T cell reporter line: Simultaneous measurement of NF-κB, NFAT and AP-1. *Journal of Immunological*

Methods **430**, 10–20 (2016).
22. Chatila, T., Silverman, L., Miller, R. & Geha, R. Mechanisms of T cell activation by the calcium ionophore ionomycin. *The Journal of Immunology* **143**, 1283–1289 (1989).
23. Goebeler, M.-E. & Bargou, R. C. T cell-engaging therapies — BiTEs and beyond. *Nat Rev Clin Oncol* **17**, 418–434 (2020).
24. Cribbs, A. P., Kennedy, A., Gregory, B. & Brennan, F. M. Simplified production and concentration of lentiviral vectors to achieve high transduction in primary human T cells. *BMC Biotechnology* **13**, 98 (2013).
25. Simon, B. *et al.* Enhancing lentiviral transduction to generate melanoma-specific human T cells for cancer immunotherapy. *Journal of Immunological Methods* **472**, 55–64 (2019).
26. Wolf, T. *et al.* Dynamics in protein translation sustaining T cell preparedness. *Nat Immunol* **21**, 927–937 (2020).
27. Tan, H. *et al.* Integrative Proteomics and Phosphoproteomics Profiling Reveals Dynamic Signaling Networks and Bioenergetics Pathways Underlying T Cell Activation. *Immunity* **46**, 488–503 (2017).
28. Ron-Harel, N. *et al.* Mitochondrial Biogenesis and Proteome Remodeling Promote One-Carbon Metabolism for T Cell Activation. *Cell Metabolism* **24**, 104–117 (2016).
29. Marchingo, J. M. & Cantrell, D. A. Protein synthesis, degradation, and energy metabolism in T cell immunity. *Cell Mol Immunol* **19**, 303–315 (2022).
30. Nagorsen, D. & Baeuerle, P. A. Immunomodulatory therapy of cancer with T cell-engaging BiTE antibody blinatumomab. *Experimental Cell Research* **317**, 1255–1260 (2011).
31. Wang, C. *et al.* Bioadhesive ultrasound for long-term continuous imaging of diverse organs. *Science* **377**, 517–523 (2022).
32. Hu, H. *et al.* A wearable cardiac ultrasound imager. *Nature* **613**, 667–675 (2023).
33. Liu, H.-C. *et al.* Wearable bioadhesive ultrasound shear wave elastography. *Science Advances* **10**, eadk8426 (2024).
34. Lin, M. *et al.* A fully integrated wearable ultrasound system to monitor deep tissues in moving subjects. *Nat Biotechnol* **42**, 448–457 (2024).
35. Abad, J. L. *et al.* Single-step, multiple retroviral transduction of human T cells. *The Journal of Gene Medicine* **4**, 27–37 (2002).
36. Hurt, R. C. *et al.* Directed Evolution of Acoustic Reporter Genes Using High-Throughput Acoustic Screening. *ACS Synth. Biol.* **13**, 2215–2226 (2024).
37. Cabrera, A. *et al.* The sound of silence: Transgene silencing in mammalian cell engineering. *cels* **13**, 950–973 (2022).
38. Maresca, D. *et al.* Nonlinear ultrasound imaging of nanoscale acoustic biomolecules. *Appl. Phys. Lett.* **110**, 073704 (2017).
39. Salahshoor, H. *et al.* Geometric effects in gas vesicle buckling under ultrasound. *Biophysical Journal* **121**, 4221–4228 (2022).
40. Heiles, B. *et al.* Nonlinear sound-sheet microscopy: imaging opaque organs at the capillary and cellular scale. 2024.07.31.605825 Preprint at https://doi.org/10.1101/2024.07.31.605825 (2024).
41. Chu, J. *et al.* A bright cyan-excitable orange fluorescent protein facilitates dual-emission microscopy and enhances bioluminescence imaging in vivo. *Nat Biotechnol* **34**, 760–767 (2016).

2.6 Figures

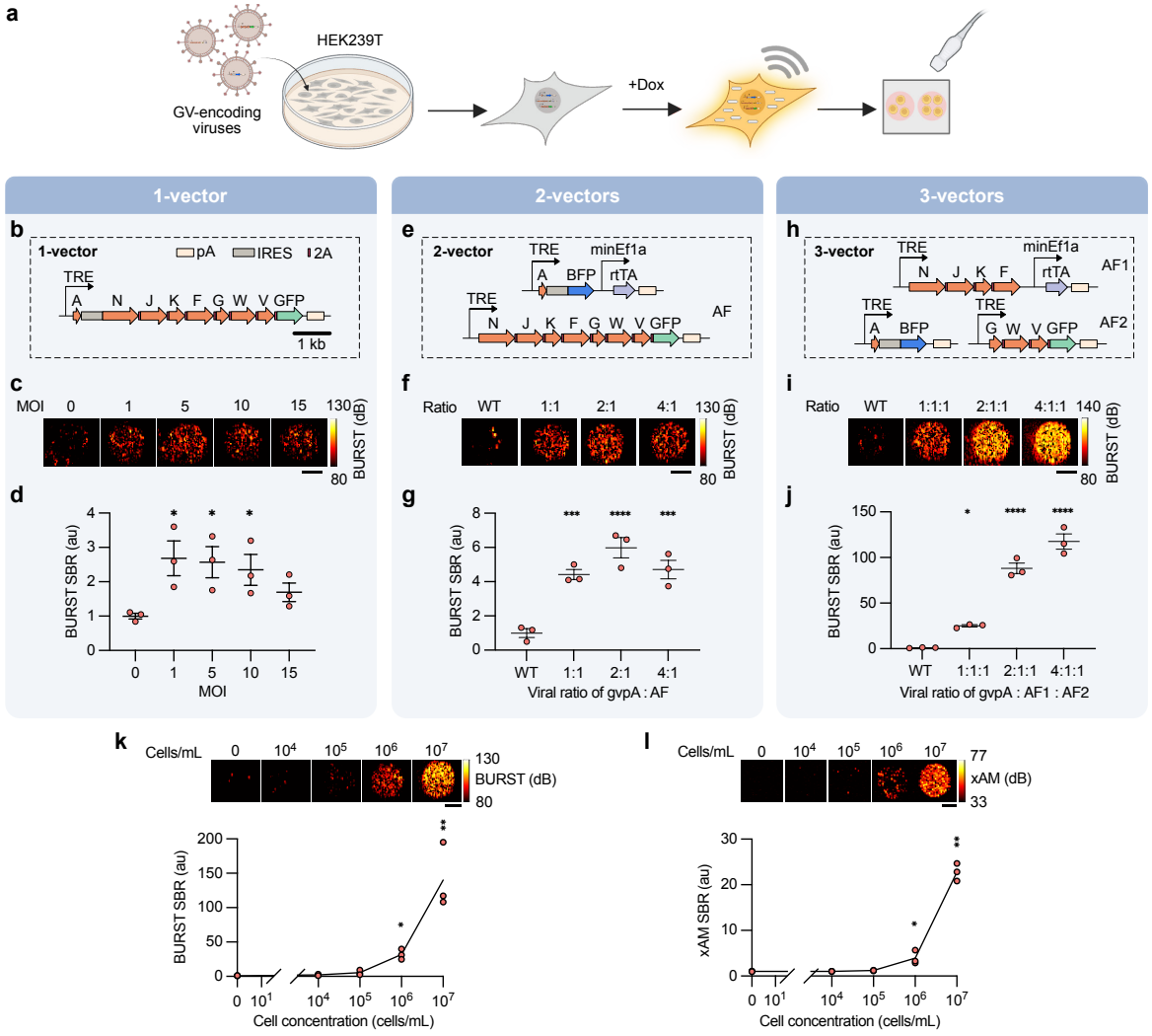

Figure 2-1: Design and optimization of multi-vector lentiviral delivery systems for robust GV expression and ultrasound imaging.

a, Schematic of the viral production and screening process. HEK293T cells are transduced with lentiviral vectors encoding GV genes, followed by doxycycline-induced GV expression for 72 hours. Cells are detached and embedded in agarose phantoms for ultrasound imaging. **b**, Schematic of a single lentiviral vector encoding all 8 GV genes. **c**, Representative BURST ultrasound images of HEK-TetON cells transduced with the single-vector virus at various multiplicities of infection (MOIs). **d**, Quantification of BURST signal-to-background ratio (SBR) in cells transduced with the single-vector virus, normalized to non-transduced cells. **e**, Schematic of two lentiviral vectors encoding GV genes and the rtTA transactivator. **f**, Representative BURST images of HEK293T cells transduced with the two-vector system at a total MOI of 10, with varying ratios of *gvpA* virus to assembly factor (AF) virus. **g**, Quantification of BURST SBR in cells from transduced with (**e**). **h**, Schematic of a three-vector system encoding the GV genes. **i**, Representative BURST images of HEK293T cells transduced with the three-vector system at a total MOI of 10, with varying ratios of *gvpA* to the first assembly factor (AF1) virus and the second assembly factor (AF2) virus. **j**, Quantification of BURST SBR in cells transduced with (**h**). **k**, Representative BURST images (top) and SBR (bottom) of HEK293T cells transduced with the three-vector system at a 4:1:1 ratio and sorted by fluorescence, shown as a function of cell concentration. **l**, Representative xAM images (top) and corresponding SBR (bottom) of the same cells as panel (**k**), shown as a function of cell concentration. For panels (**d, g, j**), statistical comparisons to non-transduced controls were performed using Fisher's least significant difference (LSD) test. For panels (**k-l**), comparisons were made against the "no cells" control using Kruskal-Wallis test. P-values from left to right: (**d**): 0.0017, 0.0165, 0.0333; (**g**): 0.0006, <0.0001, 0.0004; (**j**): 0.0107, <0.0001, <0.0001; (**k**): 0.0137, 0.001; (**l**): 0.0285, 0.0026. T-values from left to right: (**d**): 3.079, 2.877, 2.467; (**g**): 5.405, 7.878, 5.859; (**j**): 3.308, 11.98, 16.04; Df (**d**): 10; (**g**): 8; (**j**): 8; Z-values from left to right: (**k**): 2.465, 3.286; (**l**): 2.191, 3.012. Significance levels: *$p < 0.05$, **$p < 0.01$, ***$p < 0.001$, ****$p < 0.0001$; nonsignificant data points are not marked. For (**d, g, j**), error bars represent mean ± s.e.m. of N = 3 biological replicates. Each data point reflects the arithmetic mean of N = 2 technical replicates, unless noted otherwise. For (**k, l**), N = 3 replicates from independent dilution series. Scale bars for all ultrasound images represent 1 mm. au: arbitrary units. Dox: doxycycline.

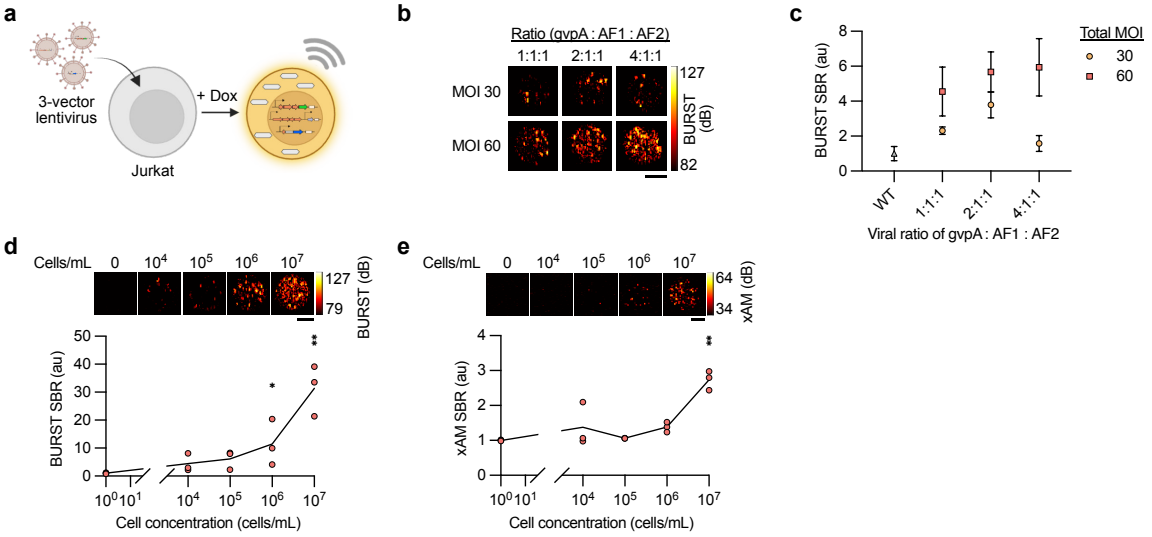

Figure 2-2: Adaptability of lentiviral GV gene delivery and ultrasound imaging of immune cells.
a, Schematic of doxycycline-inducible GV expression in Jurkat cells transduced with three lentiviral vectors encoding the GV gene cluster. **b**, Representative BURST ultrasound images of Jurkat cells transduced with different total MOIs and three ratios of *gvpA* to assembly factor (AF1 and AF2) viruses. **c**, Quantified BURST signal in Jurkat cells from panel (**b**), normalized to wild-type (WT) Jurkat cells. **d**, Representative BURST images (top) and corresponding signal quantification (bottom) of Jurkat cells transduced with the three-vector lentivirus system (MOI 60) at a 4:1:1 ratio. Cells were sorted by fluorescence expression and imaged at varying cell concentrations to measure imaging detection limit. **e**, Representative xAM images (top) and signal quantification (bottom) of the same sorted cell line from panel (**d**), shown as a function of cell concentration. Statistical comparisons for panel (**c**) were performed using Fisher's LSD test comparing each condition to WT. Statistics for MOI 60 from left to right: p = 0.0241, 0.005, 0.0034; t = 2.529, 3.328, 3.519; df = 14 (for all). Statistical comparisons for panels (**d, e**) were performed using Kruskal-Wallis test, comparing each condition to the "no cells" control. Statistics for (**d**) from left to right: p = 0.0285, 0.001, z = 2.191, 3.2386. Statistics for (**e**): p = 0.0026, z = 3.012. Significance levels: *$p<0.05$, **$p<0.01$, ***$p<0.001$, ****$p<0.0001$; nonsignificant data points are not marked. Error bars in (**c**) represent mean ± s.e.m. of N = 3 biological replicates. N = *3* replicates from independent dilution series for (**d**) and (**e**). Each data point is the arithmetic mean of N = 2 technical replicates. All ultrasound image scale bars represent 1 mm.

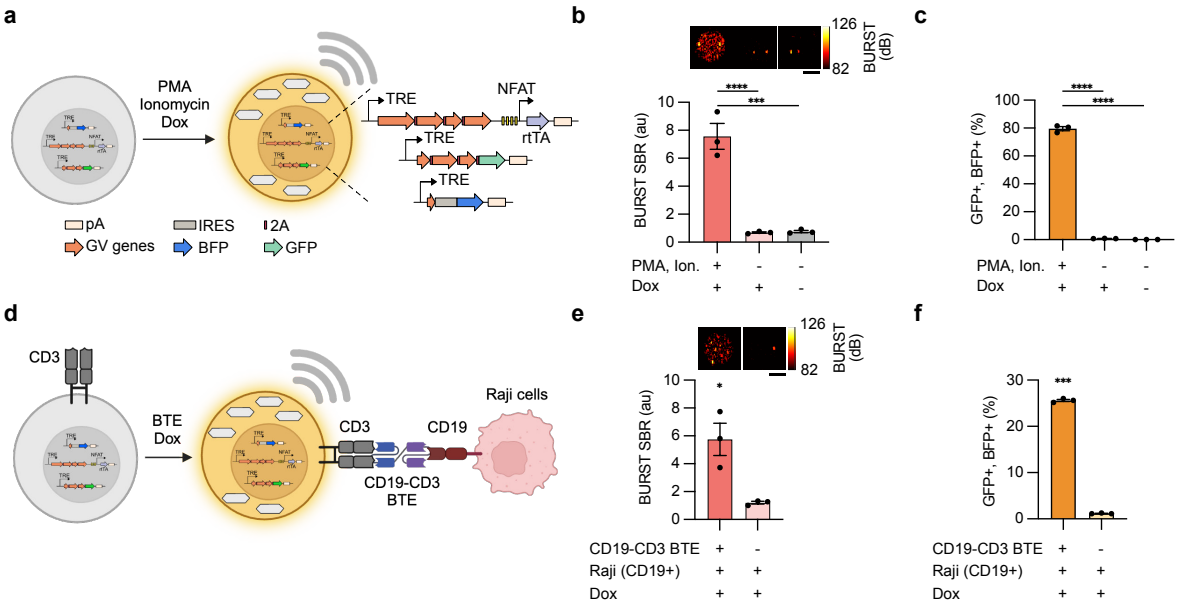

Figure 2-3: Activation-dependent GV expression enables ultrasound imaging of T cell activity.
a, Schematic of lentiviral vectors designed to report T cell activity state by expressing GVs downstream of the NFAT promoter. T cell activation is chemically induced by incubating cells with PMA and ionomycin, which trigger the NFAT promoter to express rtTA, and in the presence of doxycycline, activate transcription of GV genes. **b**, Representative BURST images (top) and signal quantification (bottom) of Jurkat cells transduced with the vectors in panel (**a**) with or without chemical activation, normalized to wild-type (WT) cells (not shown). **c**, Percentage of Jurkat cells in panel (**b**) expressing both fluorescent reporters (GFP and BFP), with and without activation. d, Imaging T cell activation in response to CD19-CD3 BTE-mediated engagement with CD19+ Raji cells, using cells engineered with the vectors shown in (**a**). **e**, Representative BURST images (top) and signal quantification (bottom) of Jurkat cells engineered to express GVs upon receptor-mediated activation in the presence of Dox. f, Percentage of cells from panel (**e**) expressing both fluorescent reporters (GFP and BFP), with and without receptor engagement. Statistical comparisons for (**b, c**) were performed using Fisher's LSD test, comparing the PMA, Ion+ and Dox+ condition against the other two conditions. (**b**) from left to right: p = <0.0001, 0.0001; t = 9.116, 9.028. df = 6, 6. (**c**) from left to right: p = <0.0001, <0.0001; t = 65.96, 66.60. df = 6, 6. Statistical comparisons for (**e, f**) were performed using ratio paired two-tailed t tests. (**e**): p = 0.0322, t = 5.434, df =2. (f): p = 0.0002, t = 67.34, df =2. Significance levels: *p<0.05, **p<0.01, ***p<0.001, ****p<0.0001. Error bars represent mean ± s.e.m. of N = 3 biological replicates. Each data point represents the arithmetic mean of N = 2 technical replicates. Scale bars for all ultrasound images represent 1 mm. Ion.: ionomycin.

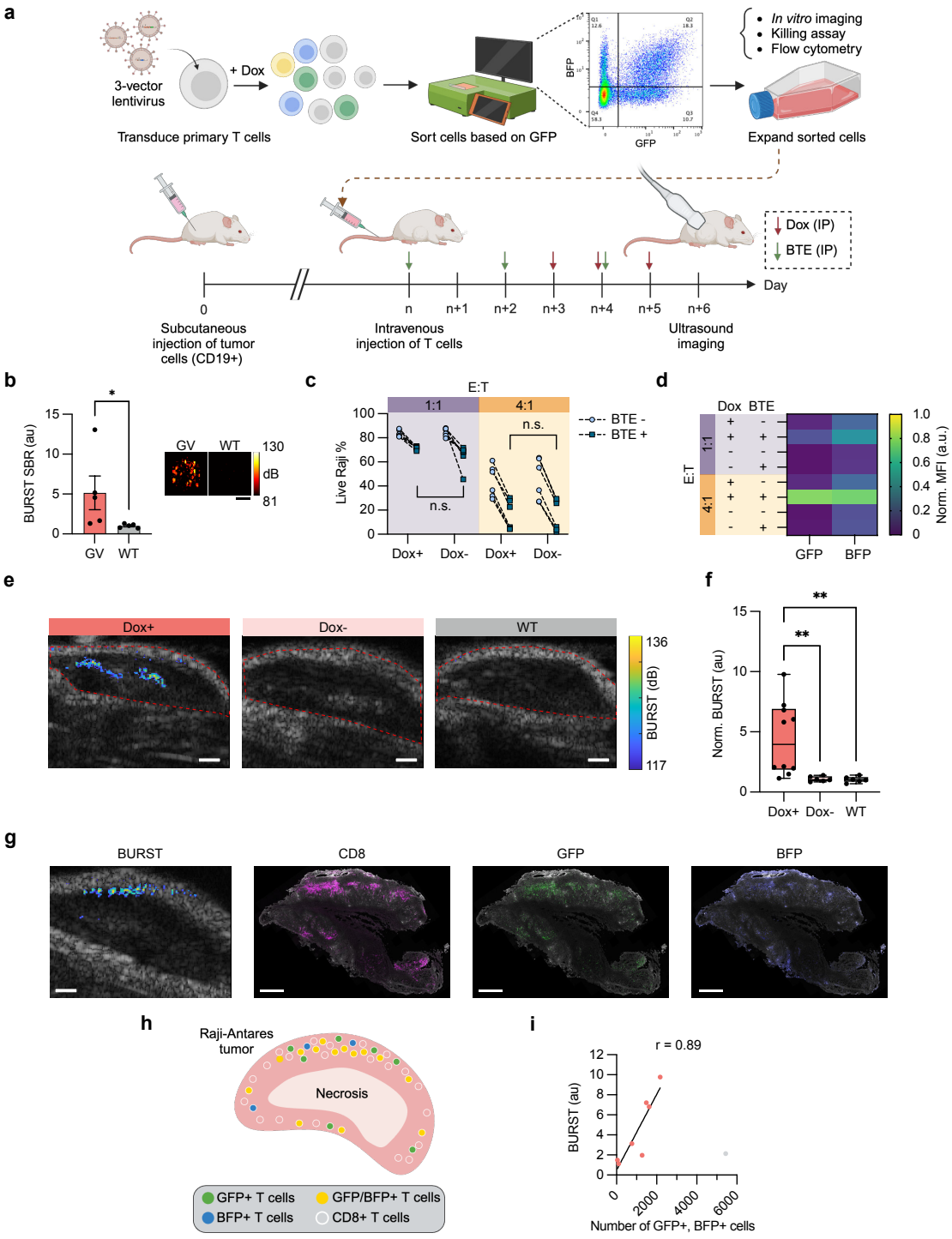

Figure 2-4: *In vivo* tracking and functional assessment of primary T cells engineered to express GVs.
a, Workflow for engineering T cells isolated from human PBMCs to express doxycycline-inducible GVs and imaging BTE-mediated homing of cytotoxic T cells into target tumors. Top: T cells are transduced with the 3-vector lentiviral system, and GFP expressing cells are sorted to select for transduction of the assembly factor vectors. The cells are then expanded *in vitro* for downstream characterization and *in vivo* injections. Bottom: T cells are systemically administered to immunocompromised mice bearing subcutaneous CD19+ Raji cell tumors, accompanied by intraperitoneal (IP) injections of BTE every 48 hours and IP

injections of doxycycline for 72 hours prior to ultrasound imaging. **b**, BURST SBR (left) and representative images (right) of GV-expressing and WT T cells. Paired one-tailed t test, p = 0.0115, t = 3.592, df = 4. Error bars represent mean ± s.e.m. of N = 5 PBMC donors; each data point is the arithmetic mean of N = 3 technical replicates. **c**, Percentage of live Raji cells in a cytotoxicity assay, where T cells are co-cultured with CD19+ Raji cells at effector-to-target (E:T) ratios of 1:1 and 4:1. Welch's two-tailed t-test, p (from left to right) = 0.1535, 0.9973, t (from left to right) = 1.668, 0.0034, df (from left to right) = 5.244, 9.935, N = 6 biological replicates (2 PBMC donors and 3 replicates per donor). d, GFP and BFP fluorescence measurements from (**c**), normalized to the maximum mean fluorescence intensity (MFI) of each reporter. **e**, BURST images overlaid on anatomical B-mode grayscale images of representative Raji tumors in mice injected with GV-expressing T cells, either Dox-induced or uninduced, and mice injected with WT T cells. Red lines indicate tumor boundary used for signal quantification. **f**, Quantification of BURST signal inside tumors. Center line, median; box limits, quartiles; whiskers**,** min to max. Unpaired Welch's two-tailed t test, Dox+ vs. Dox-, p = 0.0067, t = 3.483, df = 9.149; Dox+ vs. WT, p = 0.0063, t = 3.525, df = 9.194. N = 10 mice for Dox+, N = 6 for Dox-, N = 6 for WT. g, Histology of an example tumor infiltrated by GV-expressing T cells and its corresponding BURST image. White: Raji-Antares cells; Magenta: CD8+ cytotoxic T cells; Green: GFP+ T cells; Blue: BFP+ T cells. h, Schematic of T cell distribution in the Dox-induced tumor from (**g**). **i**, Correlation of the BURST signal within tumors with the absolute numbers of GFP+ and BFP+ T cells in corresponding histological sections. Pearson correlation: r = 0.89, p = 0.0072 (two-tailed), N = 7 mice. One mouse (gray data point, mouse 3 in **Fig. 2-S7a**) was excluded due to a significant number of T cells located outside the imaging plane whose GV expression was not captured by BURST (see **Fig. 2S-8**). All scale bars represent 1 mm.

2.7 Supplementary Figures

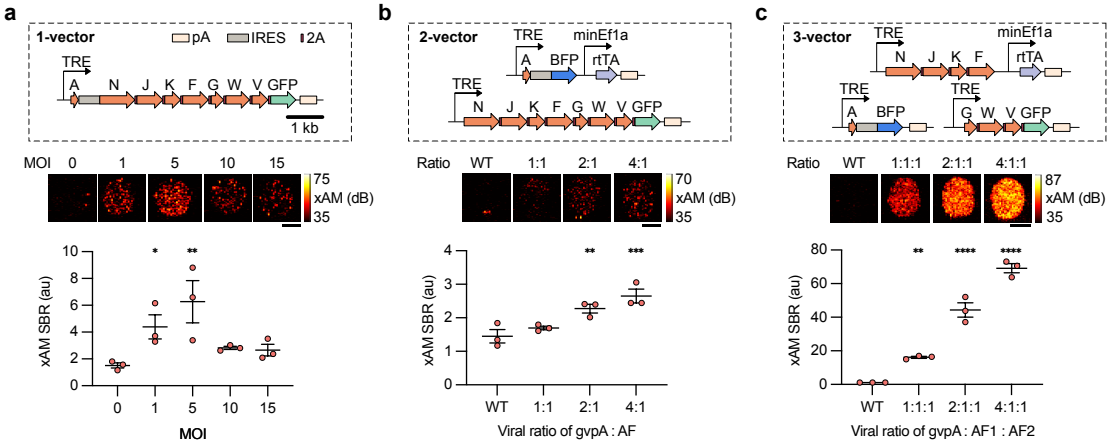

Figure 2-S1: xAM imaging of HEK293T cells expressing GVs using different lentiviral vector designs.
a, xAM imaging of HEK-TetON cells transduced with the single lentiviral vector encoding all necessary GV genes, shown at increasing MOIs. **b**, xAM imaging of HEK293T cells transduced with the two-vector lentiviral system at increasing ratios of gvpA to assembly factors (AFs). **c**, xAM imaging of HEK293T cells transduced with the three-vector lentiviral system at increasing ratios of gvpA to AF1 and AF2 vectors. Statistical comparisons to non-transduced (WT) controls were performed using Fisher's LSD test. P-values from left to right: (**a**): 0.0361, 0.0025; (**b**): 0.0065, 0.0007; (**c**): 0.0033, <0.0001, <0.0001. T-values from left to right: (**a**): 2.420, 4.007; (**b**): 3.647, 5.312; (**c**): 4.140, 11.89, 18.73. Df: (**a**): 10; (**b**): 8; (**c**): 8. Significance levels: *$p < 0.05$, **$p < 0.01$, ***$p < 0.001$, ****$p < 0.0001$; nonsignificant data points are not marked. Error bars represent mean ± s.e.m. of N = 3 biological replicates. Each data point reflects the arithmetic mean of N = 2 technical replicates. Scale bars for all ultrasound images represent 1 mm. au: arbitrary units.

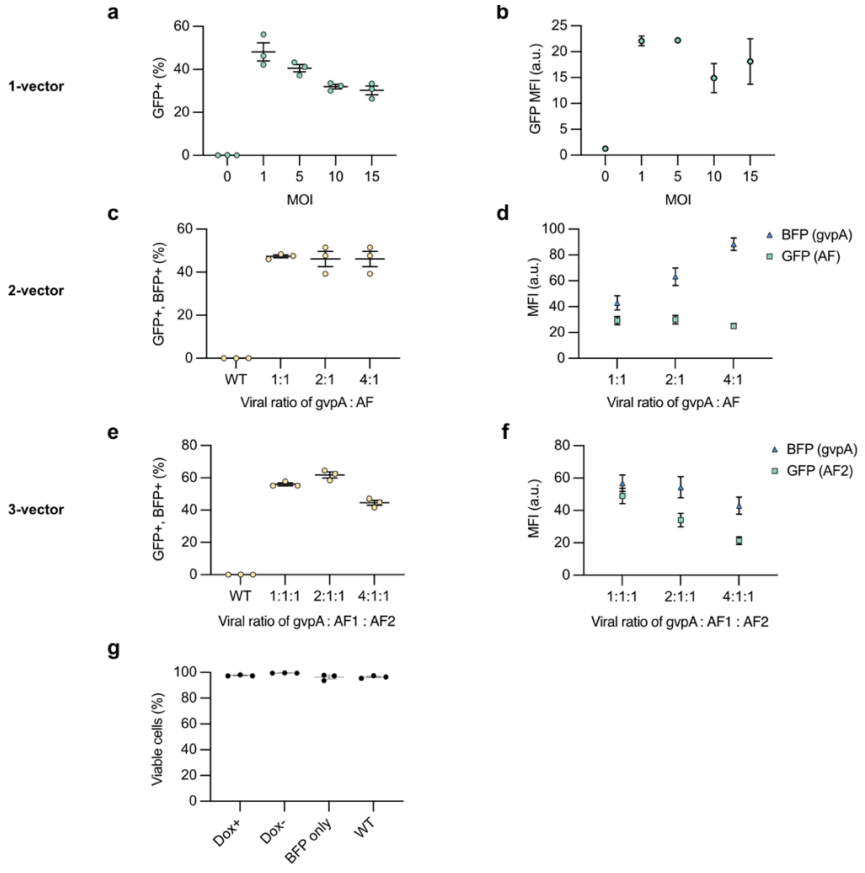

Figure 2-S2: Flow cytometry characterization of HEK293T cells transduced with various lentiviral designs encoding GV genes.

a-b, Percentage of HEK-TetON cells transduced with the single-vector virus that express GFP, the marker for transduction and their mean fluorescence intensity (MFI). **c-d,** Percentage of HEK293T cells transduced with the two-vector lentivirus system, expressing both GFP and BFP, markers for double transduced cells, and their MFI. **e-f**, Percentage of HEK293T cells transduced with the three-vector lentivirus system expressing GFP and BFP, markers for triple transduced cells, and their MFI. **g,** Percentage of live cells transduced with the three-vector lentivirus system at a 4:1:1 ratio (gvpA : AF1 : AF2) and sorted for triple-transduction, compared to cells transduced with a control virus constitutively expressing BFP at the same total MOI of 10, and WT cells. Statistical comparisons were made using Fisher's LSD test comparing the GV-expressing cells (Dox+) to uninduced cells (Dox-), the BFP control line, and wild-type (WT) cells. All p- values were non-significant. P-values from left to right: 0.1017, 0.2189, 0.3020. Error bars represent mean ± s.e.m. of N = 3 biological replicates.

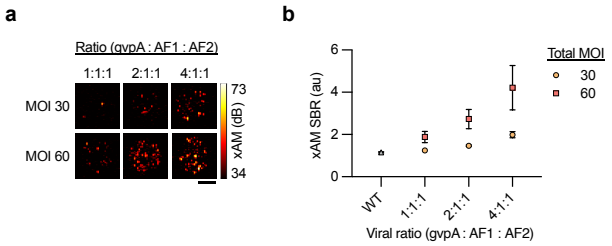

Figure 2-S3: xAM imaging of Jurkat cells transduced with the 3-vector lentivirus system at varying MOIs.
a-b, xAM imaging of Jurkat cells transduced with three lentiviral vectors encoding all necessary GV genes, shown at different vector ratios and total MOIs of 30 and 60. Statistical comparisons for panel (**b**) were performed using Fisher's LSD test comparing each condition to WT. P-values smaller than 0.5: MOI 60 (2:1:1): 0.0257; MOI 60 (4:1:1): 0.0003. Error bars represent mean ± s.e.m. N = 3 biological replicates. Each data point represents the arithmetic mean of N = 2 technical imaging replicates. All ultrasound image scale bars represent 1 mm.

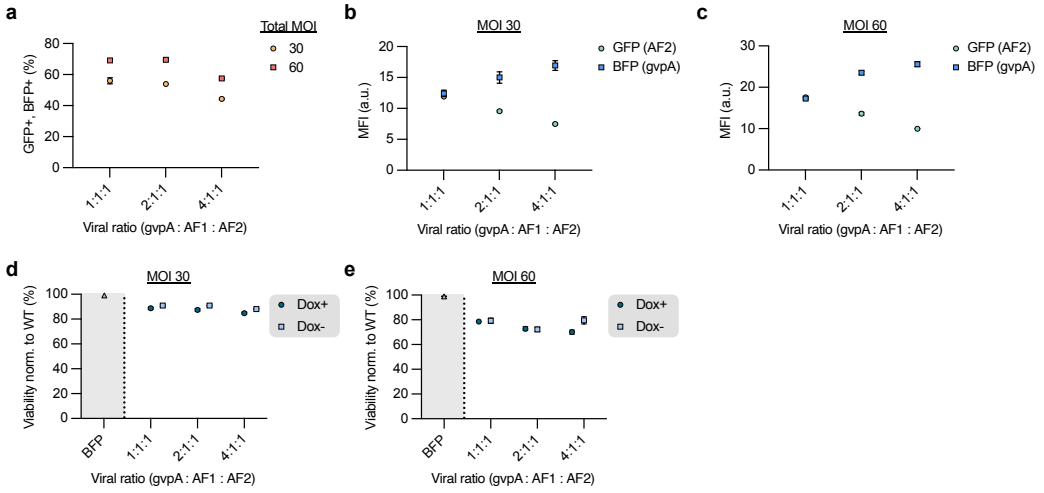

Figure 2-S4: Flow cytometry analysis of Jurkat cells expressing GVs.
a, Percentage of Jurkat cells transduced with all three GV lentiviruses that express both GFP and BFP. **b-c,** Mean fluorescence intensity (MFI) of GFP and BFP expression in the cells from panel (**a**). **d-e**, Cell viability of Jurkat cells transduced with GV-expressing lentiviruses at MOIs of 30 (**d**) and 60 (**e**), with and without doxycycline induction, and Jurkat cells transduced with a virus constitutively expressing BFP at the same MOIs. Error bars represent mean ± s.e.m. of N = 3 biological replicates.

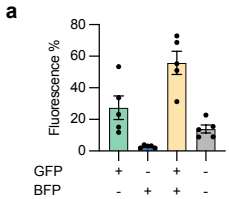

Figure 2-S5: Characterization of sorted T cell subpopulations using fluorescent transduction markers.
a, Flow cytometry analysis of doxycycline-induced and sorted T cells shows that the majority of T cells express both lentiviral transduction markers, GFP and BFP, four days after sorting. As the cells were sorted mainly based on GFP expression (assembly factor viral vectors), a smaller subpopulation expresses only GFP without BFP, the marker for the gvpA-encoding viral vector. Error bars represent mean ± s.e.m. of N = 5 PBMC donors.

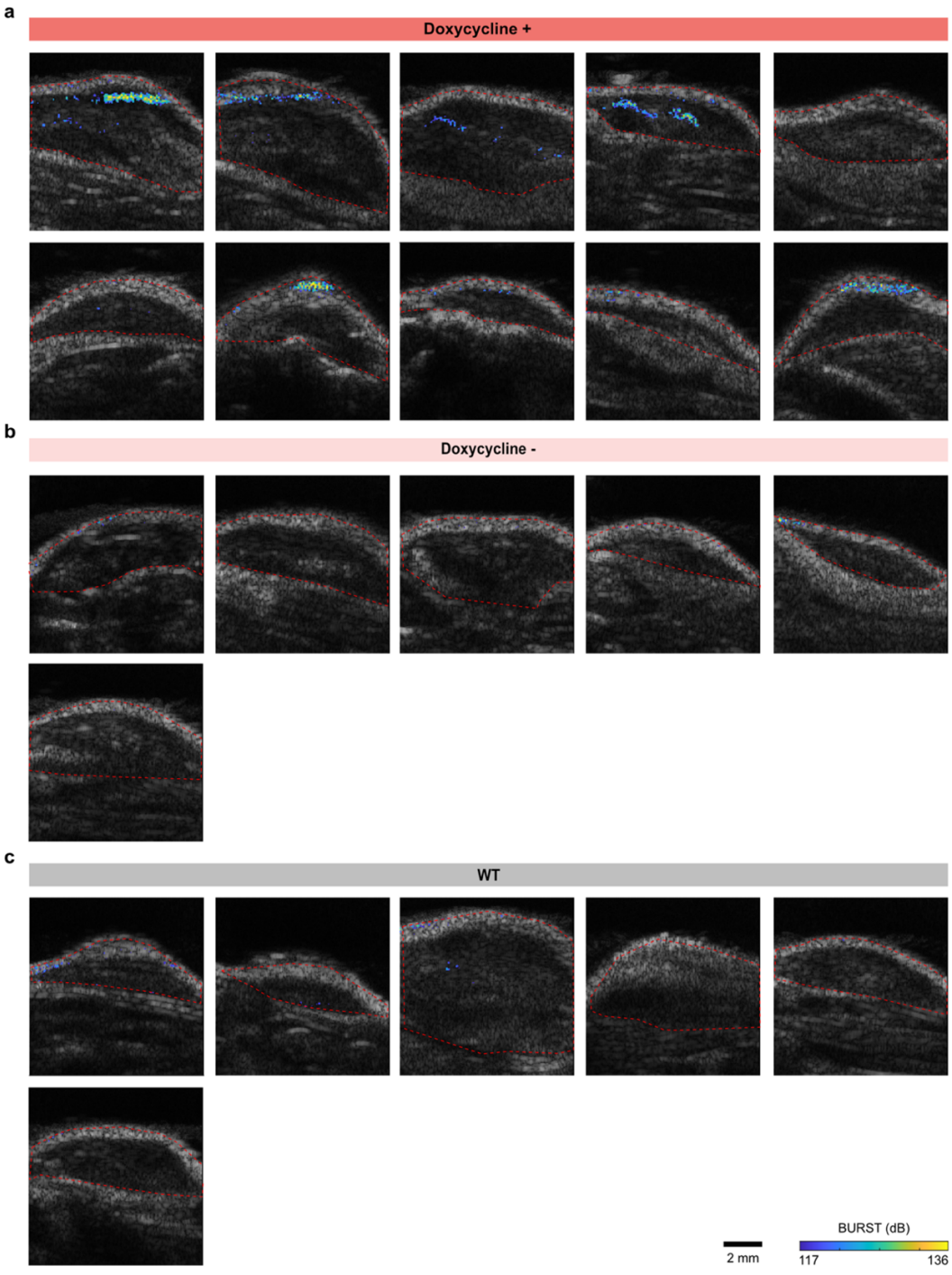

Figure 2-S6: Ultrasound imaging of Raji tumors infiltrated with T cells.
Representative BURST images (colormap) overlaid on anatomical B-mode images (grayscale) of subcutaneous Raji tumors, with each image representing a different mouse. **a**, Tumors from mice infused with virally transduced T cells, induced with doxycycline for 3 days to express GVs. **b**, Tumors from mice infused with transduced T cells but left uninduced. **c**, Tumors from mice infused with wild-type (WT) T cells.

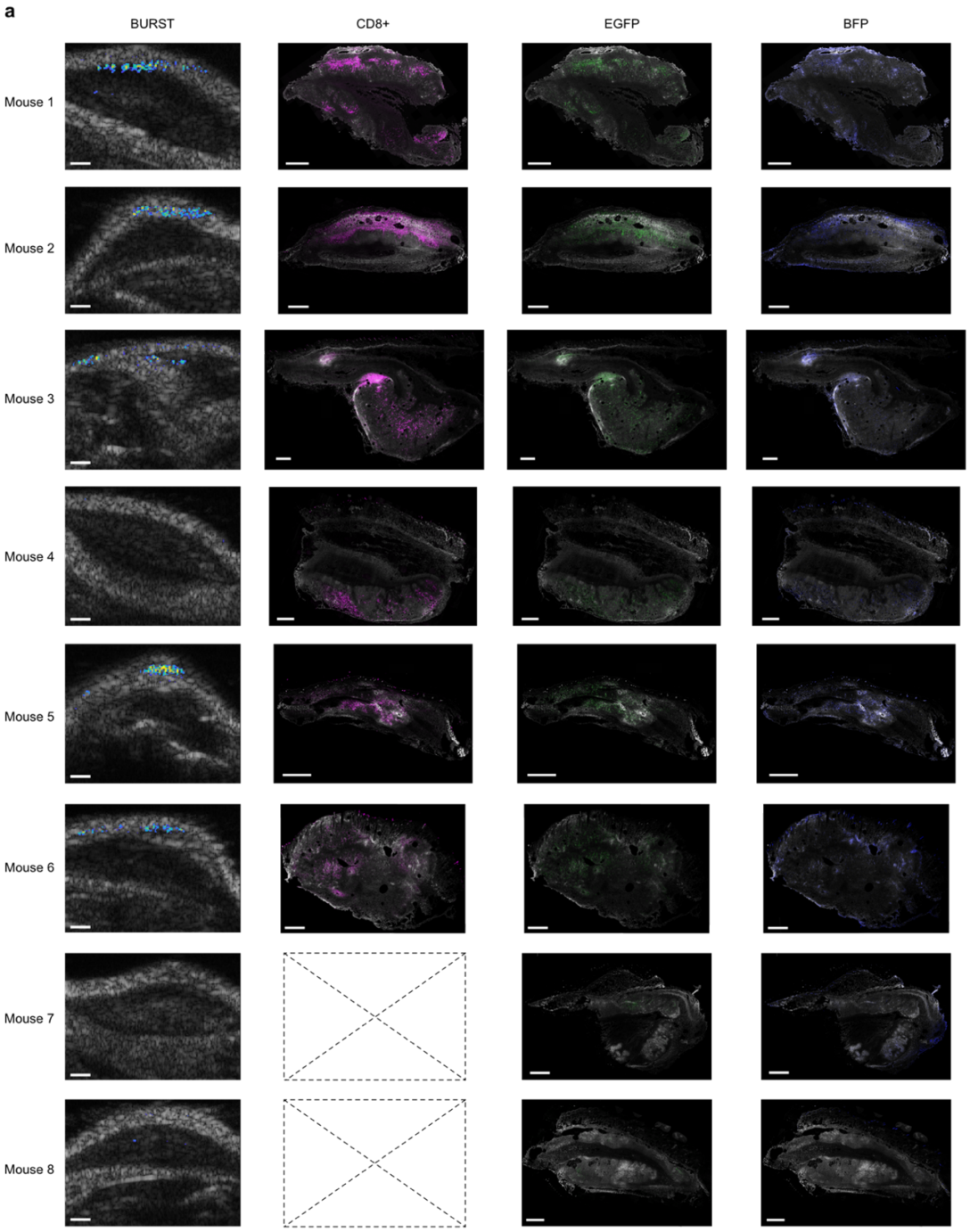

Figure 2-S7: Histological validation of T cell infiltration in tumors.
a, Ultrasound images (BURST overlaid on B-mode) of doxycycline-induced, GV-expressing T cells in Raji-Antares tumors, alongside corresponding histology showing cytotoxic CD8+ T cells, GFP+ T cells, and BFP+ T cells. Mice 7 and 8 were not processed for anti-CD8 staining due to a negligible presence of GFP/BFP-expressing T cells. Note that the histology and ultrasound images are not an exact spatial match, but are within 1 mm of each other. White: Antares; Magenta: anti-CD8; Green: GFP; Blue: BFP. All scale bars represent 1 mm.

2.8 Supplementary Material

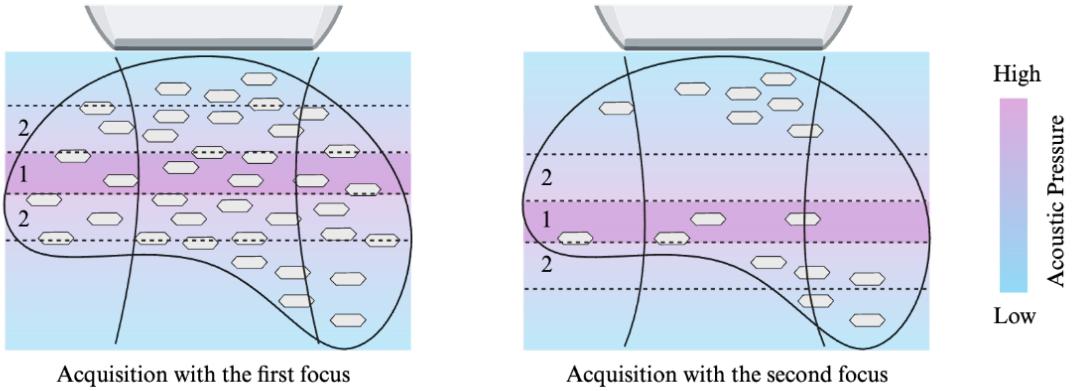

Figure 2-S8: Out-of-focus partial collapse in BURST imaging with a linear array transducer.
BURST imaging with a linear array transducer generates a focused ultrasound beam, with the highest acoustic pressure at the center of the focus (zone 1). One limitation of this method is the potential for collapsing GVs outside the focus of imaging (zone 2) at lower pressures, without producing a detectable BURST signal. While varying the focus to different depths allows us to capture some of the collapse-based nonlinear scattering, this method of imaging may not be perfectly capturing GV expression throughout the entire tumor. A potential solution would be to use a matrix array or row-column array transducer, which can generate a consistent axial pressure field along the ultrasound beam.

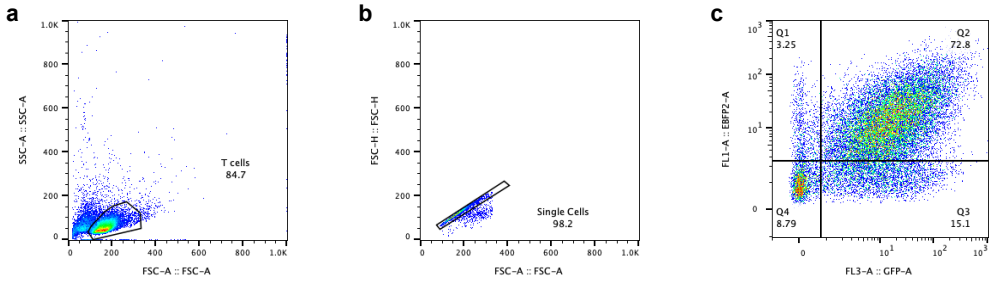

Figure 2-S9: Flow cytometry gating strategy.
Flow cytometry analysis of representative T cells transduced with the 3-vector GV expressing lentiviral vectors and induced with doxycycline. **a**, Cells are selected based on their FSC-SSC scattering. **b**, Within the "T cells" subpopulation, single cells are selected based on their FSC-H and FSC-A scattering. **c**, Within the "Single Cells" subpopulation, a threshold for each fluorescence channel is chosen based on wild-type/unstained controls. The thresholds are applied to all samples within a single experiment.

Plasmid	**Usage**
pLV-TRE3G-GvpA-IRES-NJKFGWV-mEGFP	1-vector lentiviral GV expression
pLV-TRE3G-NJKFGWV-mEGFP	2-vector lentiviral GV expression (AF)
pLV-TRE3G-GvpA-IRES-BFP-minEF1a-rtTA	2-vector lentiviral GV expression (*gvpA*)
pLV-TRE3G-NJKF-minEf1a-rtTA	3-vector lentiviral GV expression (AF1)
pLV-TRE3G-GWV-mEGFP	3-vector lentiviral GV expression (AF2)
pLV-TRE3G-GvpA-IRES-BFP	3-vector lentiviral GV expression (*gvpA*)
pLV-TRE3G-NJKF-NFATx4-rtTA	Activity-dependent GV expression
pLV-TRE3G-mScarlet-Ef1a-rtTA-BFP	HEK-TRE cell Constitutive BFP expression
pLV-Ef1a-rtTA-HygR-WPRE	HEK-TetON cell line
pEf1a-rtTA-Antares1	Raji-Anatares cell line
pCMVR8.74	Packaging plasmid
pMD2.G	Packaging plasmid

Table 2-T1: Genetic constructs used in the study.
Sources of genetic elements: *Anabaena flos. aquae* GV gene cluster : M. G. Shapiro; NFATx4: pSIRV-NFAT-GFP (Addgene #118031); Antares: pNCS-Antares (Addgene #74279); Lentivirus packaging plasmids: pCMVR8.74 (Addgene #22036), pMD2.G (Addgene #12259).

C h a p t e r 3

DEEP-TISSUE ULTRASOUND IMAGING OF IN SITU CELLULAR FUNCTION USING ACOUSTIC REPORTER GENES

Shivaei, S., Cheung, K.Y.M., Yadav, A., Hurvitz, I.U., Lee, S., Revilla, J., Rabut ,C., Crialdo-Hidalgo, E., Zhang, R., Shapiro, M.G. 2025. Deep-brain imaging of activity-dependent gene expression. *In preparation*.

3.1 Introduction

Advances in fluorescence microscopy have enabled real-time visualization of gene expression and cellular function with high spatial resolution in small organisms[1,2]. However, these methods are not easily adaptable to imaging live, intact tissues in larger animals due to the limited penetration depth of light, which restricts imaging to just a few hundred micrometers. More scalable modalities such as magnetic resonance imaging and positron emission tomography offer greater imaging depth but lack cellular-scale spatial resolution and require costly instrumentation or radioactive tracers[3]. Similarly, the poor spatial resolution of bioluminescence imaging due to light scattering obscures the detailed spatial organization of gene expression in deep tissues[4].

In contrast, ultrasound combines high spatial resolution—on the order of tens to hundreds of micrometers[5]—with deep penetration, affordability and accessibility. Recent progress in engineering gas vesicles (GVs) as acoustic reporter genes (ARGs) has expanded ultrasound's potential for molecular and cellular imaging. GVs, air-filled protein nanostructures derived from photosynthetic microbes, have been established as genetically encodable markers in mammalian cells[6,7]. Viral delivery tools have extended their use beyond immortalized cell lines into primary cells8, and recent development of enzyme- and ion-sensing GV variants have begun to connect ultrasound contrast to molecular signals[9]. Despite these advances, ARGs have yet to be adapted for *in situ* imaging of endogenous cells such as neurons or the transcriptional responses arising from their function. This challenge stems from the complexity of GV expression, which requires polycistronic encoding and the coordinated intracellular assembly of multiple proteins. In fact,

all previous work on ARGs has involved genetically modifying and sorting cells *ex vivo*, and only then injecting them into the body.

Here, we present an adeno-associated viral (AAV) system enabling the *in situ* expression of ARGs. Following intracranial delivery, we demonstrate—for the first time—that ultrasound can image *in situ* gene expression in the brain of live mice, repeatedly over time and in both 2D and 3D. By further engineering gene circuits to place GV expression downstream of immediate-early gene (IEG) promoters, we noninvasively visualize changes in IEG expression in the hippocampus resulting from an increase of neural activity during seizures, and show that these *in vivo* results strongly correlate with subsequent post-mortem histology. By leveraging ultrasound's ability to image deep tissues, this platform enables longitudinal, non-terminal imaging of dynamic gene expression in the same animal, a significant improvement over terminal histological methods and light-based imaging techniques limited by invasiveness and tissue penetration.

3.2 Results

3.2a A three-vector AAV system enables robust GV expression in primary neurons

AAVs represent the most common viral delivery system used to deliver genetic payloads into tissues such as the brain, offering cell-type specificity and tissue tropism through engineered serotypes[10–14]. Therefore, we selected AAV as the delivery vehicle for the GV gene cluster. As our initial testing platform, we selected cultured primary neurons, a non-dividing cell type that served as a prelude to *in vivo* experiments in the mouse brain. We chose these this cell typ due to its common targeting with AAVs and the high interest in imaging its gene expression in the brain.

Building on previous work on delivering a GV gene cluster into immune cells[8], we designed a three-vector AAV system expressing GVs under the control of a Tet transactivator, with each vector adhering to the ~4.8 kb packaging size limit (**Fig. 3-1a**). The smallest GV gene cluster previously shown to express functional GVs is derived from Anabaena flos-aquae, with its assembly factor genes (*gvpNJKFGWV*) comprising 4.7 kb when linked by 2A peptides for polycistronic expression. To accommodate the addition of promoters and polyA sequences, we split the assembly factor genes across two AAVs: one encoding *gvpNJK* and the transactivator rtTA (4.5 kb, ITR-ITR), and the other encoding TRE-driven *gvpFGWV* and GFP for quantifying transduction efficiency (4.2 kb, ITR-ITR). We isolated the main structural GV gene, *gvpA*, co-

expressed with RFP on a third AAV (2.6 kb, ITR-ITR), enabling independent control of its titer relative to the assembly factors. Each vector incorporated an engineered compact WPRE and poly-A sequence, CW3SL15, which occupies only a 432 bp DNA footprint, thereby minimizing packaging size. We packaged these vectors in AAV9, a serotype commonly used in neurons and the brain[16].

To test this system, we cultured mouse cortical and hippocampal neurons *in vitro* and delivered the GV gene cluster using a 5:1:1 ratio of the AAV vectors encoding *gvpA* to those encoding the two sets of assembly factors (AFs). This ratio was chosen based on prior findings that an elevated gvpA ratio enhances the nonlinear acoustic scattering of GVs[7,8]. Expression was induced by adding doxycycline (1 μg/mL) every 24 hours for 72 hours. Cells were then trypsinized, resuspended in PBS, and embedded in agarose phantoms for ultrasound imaging (**Fig. 3-1b**).

BURST, a highly sensitive nonlinear detection method for GV imaging[17], revealed a strong signal of 55.06 ± 14.59 (a.u., mean ± s.e.m.) in wells containing GV-expressing neurons, compared with 1.66 ± 0.06 (a.u., mean ± s.e.m.) in wells containing wild-type (WT) neurons (**Fig. 3-1c-d**). Phase microscopy of the cultures showed clusters of GVs[18,19] forming in the soma (**Fig. 3-1e-f**). These clusters were absent in both non-transduced cells and in cultures transduced with a constitutively expressing mCherry virus (**Fig. 3-S1a-c**). Calcein AM staining of Dox-induced and Dox-uninduced cells, as well as WT type cells, showed similar levels of metabolism across these conditions (**Fig. 3-S2**).

These results demonstrate that a multi-AAV approach can successfully deliver ARGs to non-dividing primary cells, leading them to robustly express GVs visible with ultrasound and phase microscopy.

3.2b AAV-based delivery enables longitudinal deep-brain imaging of in situ gene expression

Having validated our multi-AAV expression system *in vitro*, we set out to test its ability to deliver ARGs to *in situ* cells deep inside an opaque tissue and enable repeated imaging of gene expression in living animals over an extended period. The brain presents an ideal testing ground for this purpose, with established interest in using gene expression to visualize anatomical structures, cell types and activation. As our anatomical target, we selected the hippocampus, a tissue with a well-defined three-dimensional geometry, a location that is too deep for optical access, critical importance in healthy brain function, and involvement in diseases such as epilepsy. To address these limitations, we tested whether intracranial injection of our three-

vector AAV system into the brain could enable robust GV expression over the span of weeks to months.

To test the *in vivo* delivery of our designed AAV system, we co-injected a mix of the three viruses, delivered at a 5:1:1 ratio of *gvpA* to the assembly factor viruses, into the hippocampus of immunocompetent C57BL/6J mice. GV expression was induced via intraperitoneal (IP) injections of doxycycline, administered every 24 hours for 72 hours, after which the brain was imaged through a cranial window (**Fig. 3-2a**). As a comparison, we also injected mice with an AAV virus constitutively expressing mCherry at similar titers and injection coordinates. Using a 2D linear ultrasound probe, we saw strong BURST signal at 4.0e4 ± 1.5e4 (a.u., mean ± s.e.m., n = 6 mice) in the brain of mice injected with the GV-expressing AAVs, localized with anatomical Doppler images (**Fig. 3-2b, c and Fig. 3-S3**), while mCherry-injected mice exhibited minimal signal at 3.8e2 ± 2.4e2 (a.u., mean ± s.e.m., n = 4 mice). Interestingly, despite unilateral injection, we observed BURST signal in the contralateral side of the hippocampus, demonstrating the sensitivity of this approach to visualize gene expression even at distant sites of spread, which likely occurred via diffusion or anterograde/retrograde viral transduction.

BURST imaging with a linear transducer array enabled high-resolution visualization of GV expression in individual 2D planes of the brain. However, each BURST acquisition has the potential to collapse GVs in adjacent planes outside the imaging field, due to the elevation focus of the transducer – without capturing their nonlinear signal. Additionally, the focused parabolic acoustic beams generated by a linear array impose a shallow axial focal zone with the peak at the center of the parabola, and constrain depth resolution. To overcome these limitations and achieve volumetric imaging, we used Takoyaki 3D BURST imaging using a matrix transducer array, which can create a homogenous pressure field across the elevation and depth axis of the ultrasound probe[20]. This method allowed us to image the entire hippocampus—from anterior to posterior—in a single acquisition spanning multiple millimeters in depth (**Fig. 3-2d**). By combining depth penetration with spatial coverage, Takoyaki imaging extends our platform to true 3D mapping of gene expression while preserving anatomical detail.

To evaluate the efficiency and cell-type specificity of AAV-mediated GV delivery, we performed histological analysis on brains expressing ARGs. Among fluorescent cells, 59.4 ± 2.8% (mean ± s.e.m., n = 4 mice) were both GFP and RFP positive, indicating successful triple transduction with all three AAV vectors (**Fig. 3-2e, f**). Within this population, 93.5 ± 1.0%

(mean ± s.e.m., n = 4 mice) co-localized with NeuN, confirming that the majority of BURST signal originated from neurons (**Fig. 3-2e, f**). To assess toxicity, we stained for cleaved caspase-3 and found that 12.1 ± 2.5% (mean ± s.e.m., n = 4 mice) of triple-transduced cells were apoptotic (**Fig. 3-S4**), possibly due to a combination of high levels of viral titer and GV expression.

Having established the robustness of our delivery system, we next tested whether this platform could support longitudinal imaging of gene expression. We injected the GV-expressing AAV mix into the hippocampus and implanted an acoustically transparent cranial window on top of the brain. GV expression was induced for 48 hours, imaged, and then collapsed using ultrasound. This induction-imaging cycle was repeated every two to three weeks for a total of four sessions (Fig. 2h). While some variability in expression was observed between imaging sessions, BURST signal remained present throughout the study period without evidence of time-dependent signal loss (**Fig. 3-2i, j** and **Fig. 3-S5**).

Together, these results establish, for the first time, the feasibility of using ultrasound to image *in situ* gene expression in a living brain across time. This platform enables longitudinal, tissue-wide imaging at cellular resolution, offering a powerful and non-invasive alternative to terminal histological methods.

3.2c ARGs driven by immediate early gene expression track intracellular activity

Having established imaging of *in situ* ARG expression in the brain, we aimed to develop an ultrasound marker for tracking changes in cellular function, inspired by optical markers designed to track the activity of IEGs[21–23]. While IEG-based fluorescent markers have been widely used to study traces of activity, their reliance on histological readout inherently limits them to terminal experiments. Our goal was to design and optimize an ultrasound marker of IEG expression and establish its sensitivity.

To achieve this, we focused on two IEG promoters: the widely used cFos promoter and a synthetic promoter with enhanced expression fold change, RAM, that combines a synthetic enhancer module consisting of Activator Protein 1 (AP-1) and Npas4 sites with a minimal cFos promoter[23]. To minimize leakiness and allow more precise temporal control over GV expression, we reduced the half-life of the rtTA transactivator by adding an ODC degron to its 3’ end with a GS linker, creating a variant we termed RAM-deg. We replaced the constitutive minEf1a

promoter upstream of rtTA with these activity-inducible promoters and tested their fold change of expression in HEK cells. Resting cells were compared to cells with chemically induced activity using phorbol 12-myristate 13-acetate (PMA) and ionomycin. The cells were incubated with the activity induction mix and doxycycline for 4–6 hours, then returned to regular media, and imaged 24 hours after the onset of induction (**Fig. 3-3a**).

All three promoters exhibited increased BURST signal following induction. Among them, the RAM-deg promoter produced the highest fold change in BURST signal, reaching 5.6× (**Fig. 3-3b, c**). Flow cytometry further confirmed these results, showing that RAM-deg had the lowest basal activity and the highest fluorescence expression upon induction (**Fig. 3-3d**). Based on these findings, we selected RAM-deg as our best-performing variant for activity-dependent GV expression.

To evaluate the sensitivity of the RAM-deg system, we tested its response to both the duration and concentration of activity induction. Because AP-1–mediated activation of the cFos promoter is transient—peaking within 30 minutes to ~2 hours and decaying by 4–6 hours[24,25] —we varied the duration of stimulation with the activity-inducing molecules from 15 minutes to 4 hours to determine the minimum exposure needed to drive sufficient cFos-dependent GV expression. RAM-deg–transduced cells were incubated with the inducer mix for these time intervals and imaged 24 hours after the start of induction. We found that even 15 minutes of sustained activity was sufficient to produce detectable GV expression (**Fig. 3-3e**). To assess concentration sensitivity, we incubated cells with serial dilutions of the inducer mix (1:10 to 1:1000) for 4 hours and imaged them 24 hours later. BURST signal was detectable at dilutions as low as 1:100, but not at higher dilutions (**Fig. 3-3f).**

These results establish RAM-deg as a sensitive, activity-inducible system for tracking IEG-induced transcription with ultrasound.

3.2d Ultrasound enables imaging of conditional IEG-induced gene expression in the brain during epileptic seizures

The ability to image conditional gene expression *in situ* is a powerful tool for studying dynamic cellular processes across a variety of biological contexts. IEG promoters specifically have been widely used to drive activity-dependent or stimulus-induced expression, but their use in live animals has largely relied on fluorescent reporters that require terminal histology, precluding

longitudinal studies and increasing animal usage[26–32]. To overcome these limitations, we sought to see whether our RAM-deg GV variants could serve as an ultrasound-based marker of IEG expression in the brain that enables repeated, non-invasive measurements of transient transcriptional responses in the same animal, providing a broadly applicable platform for tracking gene expression dynamics *in vivo*.

Having optimized an IEG-driven version of our virally delivered GV gene cluster in HEK cells, we adapted the system for *in vivo* use by incorporating it into an AAV backbone. Specifically, we replaced the minEf1a-rtTA element (**Fig. 3-1a**) with the RAM-deg construct, which includes a destabilized rtTA under the control of the RAM promoter (**Fig. 3-4a**). We also incorporated a constitutively expressed iRFP670 fluorescent marker[33] into the gvpA construct to serve as a transduction indicator. We verified that co-injection of this modified gvpA-encoding virus with the unmodified assembly factor viruses at a 5:1:1 ratio did not affect BURST signal in the hippocampus (**Fig. 3-S6**). To test whether this AAV system could track IEG-induced gene expression *in vivo*, we used a well-characterized model of temporal lobe epilepsy in which systemic kainic acid injections induce seizure[34,35]—a behavior previously studied using IEG-driven fluorescent reporters[23]. As a control, we confirmed by immunohistochemistry that kainic acid reliably increased cFos expression in the hippocampus, absent in saline-injected mice (**Fig. 3-S7**).

To image seizure-induced changes in gene expression, we injected the RAM-deg AAV system into the dentate gyrus of mice and performed two imaging sessions per animal. For the baseline session, we administered doxycycline and saline, followed by ultrasound imaging 24 hours later (day 1). On day 6, we induced seizures in Group A mice via intraperitoneal injection of kainic acid, while Group B mice received a second round of doxycycline and saline as a sham control (**Fig. 3-4b**). All mice were imaged again on day 7.

In Group A mice that exhibited seizure behavior, we observed a significant increase in BURST signal in the hippocampus on day 7 compared to baseline measurements taken on day 1 (**Fig. 3-4c, d**). In contrast, Group B mice that received sham injections showed no significant change in BURST signal over the same period. Histological analysis supported these findings, revealing strong GFP and RFP fluorescence in the hippocampus, particularly in the dentate gyrus, of seizure-induced mice (**Fig. 3-4e**). In sham-treated mice, fluorescence remained weak and consistent with basal levels.

Interestingly, a subset of Group A mice displayed behavioral signs of seizure, such as freezing and head bobbing, but showed no detectable BURST signal in the hippocampus (**Fig. 3-S8,** rows 6–8). Histological analysis of these animals confirmed weak GFP and RFP fluorescence, comparable to baseline expression. Across Group A, we observed a strong correlation between BURST signal and MFI of GFP and RFP in the hippocampus, including in animals with minimal signal (**Fig. 3-4f**; Pearson $r = 0.989$, $p < 0.0001$). In contrast, there was no significant correlation between BURST signal and the constitutive fluorophore iRFP670 (**Fig. 3-4g**; Pearson $r = 0.104$, $p = 0.79$).

This consistency between ultrasound imaging and histological fluorescence highlights the robustness of our system, demonstrating strong agreement with established terminal fluorescence-based readouts. These results establish the first tool for longitudinal, brain-wide imaging of conditional gene expression in a live animal. By eliminating the need for terminal histology, reducing inter-animal variability, and enabling repeated measurements in the same subject, this platform represents a major advancement for studying tissue-wide circuit dynamics over time.

3.3 Discussion

This work presents the first use of ARGs expressed *in situ* in a live animal and the first demonstration of ultrasound-based imaging of endogenous gene expression in intact tissue. Imaging gene expression directly within living organisms provides a powerful window into cellular function and dynamics, but has remained technically difficult beyond superficial tissues or *ex vivo* models. The multi-AAV system introduced here enables robust expression of GV generates strong BURST signal following intracranial injection into the hippocampus. This signal is detectable even in deep brain regions and can be captured in a single 3D acquisition. We demonstrate that this platform supports repeated imaging in the same animal over multiple weeks, surpassing the spatial and temporal limitations of conventional reporter-based optical imaging. Furthermore, by driving GV expression under the control of IEG promoters, we developed a variant of our reporter system regulated by endogenous transcription factors with minimal baseline leakiness that sensitively tracks changes in intracellular activity both *in vitro* and *in vivo*, demonstrated by imaging IEG expression in the hippocampus after epileptic seizures. Leveraging the deep penetration and non-invasiveness of ultrasound, this tool enables paired imaging of baseline and post-stimulation gene expression in the same animal, providing

an internal control that reduces animal-to-animal variability and enhances measurement reliability.

This work introduces a non-invasive approach for monitoring the expression of virally delivered genetic constructs and their dynamic changes over time—an achievement that is significantly more difficult, and often prohibitively costly, using optical methods in larger animals such as marmosets. Furthermore, this imaging platform could be extended to brain-wide monitoring of gene expression following systemic AAV delivery, enabling single-acquisition, comprehensive imaging of the entire brain. The development of a non-invasive IEG reporter also opens new possibilities for investigating dynamic processes such as memory formation within the same animal over extended time periods[29,36–39]. When paired with systemic delivery methods or transgenic models, this technique has the potential to support longitudinal, multi-organ circuit analysis at an unprecedented scale. Furthermore, integrating this system with recently developed GV-based protease and calcium sensors[9,40] paves the way for non-invasive imaging of spontaneous *in situ* molecular dynamics with both high spatial and temporal resolution.

Although we observed no overt behavioral abnormalities or widespread cytotoxicity in animals expressing GVs, further work is needed to assess the impact of GV expression on cellular physiology, ideally in a cell-type–specific manner using functional assays. Another open question is whether co-transduction efficiency of all three AAVs could become a limiting factor in the context of systemic delivery. Reducing the system to two AAVs could improve accessibility and scalability, which can be achieved through the rational engineering or screening of more compact GV gene clusters[7,41]. While we demonstrated that ultrasound can image GV expression across large brain regions, future studies should define the minimum viral dose required to resolve smaller substructures. It also remains to be seen whether GV expression efficiency is biased by regional or cell type differences—for example, whether pyramidal excitatory neurons, which are abundant in the hippocampus, are more permissive to GV expression than others. Lastly, improving the nonlinear acoustic properties of GVs through the development of engineered variants or tuning gene stoichiometry to favor elongated GV structures could further enhance imaging sensitivity and allow the use of non-collapsed based methods of GV imaging.

Altogether, this platform establishes the first genetic toolset for deep-tissue, ultrasound-based imaging of gene expression in live animals. By enabling longitudinal, non-invasive visualization

of transcriptional dynamics, it paves the way for studying cellular function over time within intact tissues and in natural physiological contexts.

3.4 Methods

Plasmid construction and molecular biology

All genetic constructs were made using either KLD mutagenesis or Gibson Assembly with enzymes from New England BioLabs. The plasmids and their corresponding genetic material sources are detailed in Supplementary Table 1. Constructs were cloned into NEB Turbo Competent E. coli (High Efficiency). Fluorescent reporters referred to as GFP, RFP, and iRFP670 in the text correspond to mEGFP, mScarlet-I, and emiRFP670 respectively. All AAV transgenes were packaged into AAV9 plasmids, and both packaging and titering were outsourced.

Dissection of embryonic mouse neurons

All dissection tools were autoclaved before use to maintain sterility. Tissue culture-treated 24-well polystyrene plates were coated with poly-D-lysine (PDL, 100 µg/mL, Gibco) diluted to 50µg/mL in sterile DPBS, at room temperature for 1 hour. Poly-D-lysine solution was then removed, washed twice with molecular biology-grade water and left to dry in the biosafety cabinet prior to seeding.

A pregnant female mouse on embryonic day 18 (E18, Charles River Laboratories) was euthanized. A skin incision was made and pups were extracted while still enclosed in membranous sacs and placed in a 10 cm dish on ice. Under a sterile hood, pups were decapitated, and brains were extracted one at a time, immediately placed in cold HBSS. The cortex and hippocampus from each hemisphere were dissected and stored in cold HBSS. Tissue was then cut into 3–4 small pieces using fine forceps. For dissociation, tissue fragments were incubated in papain (Worthington Biochemicals PAP2/LK003178, diluted to 15–20 U/mL in 1X PBS) for 20–30 minutes at 37 C, with gentle shaking or flicking at regular intervals. Digestion was stopped by transferring tissue into 10% FBS in HBSS, while minimizing shear stress. Cells were then triturated 10–12 times. The suspension was centrifuged at 100 × g for 8 minutes. The resulting pellet, containing a homogeneous suspension of single cells, was resuspended in neuronal culture media containing Neurobasal Plus media (Thermofischer, #A3582901), 1X B27 Plus supplement (Thermofischer, #A3653401), and 1X penicillin/streptomycin. Cells were counted by 1:1 dilution in AO/PI dye. 2.5×10^5 cells were plated in each well of a pre-coated 24 well plate. The culture media was fully replaced with pre-warmed media on day in vitro 1 (DIV 1), followed by half-media changes every four days thereafter.

Primary cultured neuron transduction and induction

Cultured neurons were transduced on DIV 5 with either 1.4 × 106 GC of the three GV-encoding AAV9 viruses or 1 × 106 GC of a single mCherry-encoding AAV9 virus (Addgene). Beginning on DIV 13, neurons were induced every 24 hours with doxycycline (1 μg/mL). Imaging was performed on DIV 16.

Phantom loading of cultured neurons

On the day of imaging, cells were trypsinized using 2.5% trypsin for 5 minutes at 37°C. They were then gently detached from the culture dish and resuspended in 1X PBS containing DNase I (100 μg/mL) to prevent clumping. The cell suspension was then centrifuged at 300 × g for 5 minutes, and the supernatant was carefully removed. Cells were then briefly mixed at a 1:1 ratio with 1% melted agarose in 1X PBS at 42°C. The agarose solution was prepared at least 24 hours in advance to eliminate bubbles. The cell-agarose mixture was then loaded into agarose phantoms. Each well of a 12-well plate was divided across two wells of the phantom, yielding a final cell concentration of approximately 10 million cells/mL.

In vitro IEG induction

HEK293T cells were transduced with the activity-dependent three vector lentiviral system, using previously established methods for transduction of lentivirally-encoded GVs8. Cells were seeded ~24 hours before induction DMEM (Corning, 10-013-CV) with 10% FBS (Gibco) and 1X penicillin/streptomycin at 37 °C, 5% CO2, until they reached 80-90% confluence. They were then incubated in ionomycin (1.3 μM), phorbol myristate acetate (PMA, 100 ng/mL), and doxycycline (1 μg/mL) supplemented DMEM at 37 °C, 5% CO2 for 4 hours. The inducers were removed, and the cells were washed once in 1X PBS and maintained in doxycycline (1 μg/mL) supplemented DMEM media for 20 hours before ultrasound imaging and flow cytometry. In titration and time induction experiments, the duration of induction and concentration of inducers were varied, as shown in Fig. 3e, f.

Phantom loading of HEK293T cells

On the day of imaging, cells were trypsinized with 0.25% trypsin and resuspended in regular DMEM. They were briefly mixed at 1:1 dilution at 42°C with 1% melted agarose in 1X PBS prepared at least 24 hours earlier, and loaded into agarose phantoms at a final concentration of 25 million cells/mL.

Animals

C57BL/6J mice were obtained from Jackson Lab and bred at Caltech facilities. Animals were housed in a 12 h light/dark cycle and were provided with water and food ad libitum. A mixed population of male and female mice, chosen randomly, were used in studies. All experiments were conducted under a protocol approved by the Institutional Animal Care and Use Committee of the California Institute of Technology.

Intracranial injection

Solutions of the three GV-encoding AAV9 viruses, mixed at a 5:1:1 ratio of the gvpA-encoding virus to the assembly factor viruses, or a single AAV9 encoding mCherry under an Ef1a promoter were injected into the hippocampus of C57BL/6J mice at 8-11 weeks of age using a pulled glass needle coupled with a motorized pump at 70 nL/second using a stereotaxic frame. All injections were done at coordinates of -2.1 mm anterior-posterior (AP), -1.5 mm medio-lateral (ML), -1.8 mm dorso-ventral (DV) with respect to bregma. The needle remained in place after injection for 5 min to avoid backflow along the needle tract. The total volume of injection was 3 uL, for a total viral load of 3e10 to 3e11 genome copy (GC) number, measured by qPCR titer. For each batch of virus, an initial test experiment was performed to determine the amount of time needed to wait after injection before a significant BURST signal was detected. This time varied between 3 to 8 weeks, depending on the batch of virus, before the first round of ultrasound imaging.

Cranial window surgery

All ultrasound images of mice that were imaged with ultrasound only once were done with the skull removed. Specifically, mice were anesthetized under 1-2.5 % isoflurane and injected subcutaneously with mannitol to reduce inflammation. A craniotomy was performed from AP -0.5 mm to AP -3.5 mm and from ML -2.5 mm to ML +2.5 mm using a micro-drill steel burr. Care was taken to not damage the dura.

Acoustically transparent window implants

All mice that were imaged more than once, had their skull removed and replaced with an acoustically transparent window. Specifically, after craniotomy, the skull flap was replaced with a TPX (polymethyl pentane) window of similar size and fixed in place using a UV-curable composite (Tetric EvoFlow) and dental metabond cement (Patterson Dental Company). There was a minimum of one week before the implant surgery and the ultrasound imaging to ensure there are no bubbles under the TPX window.

Doxycycline administration

For single-time imaging experiments, mice received intraperitoneal injections of doxycycline hydrochloride (HCl) at 4 mg/kg in saline every 24 hours for 72 hours. For repeated imaging experiments, mice were injected with doxycycline HCl every 24 hours for 48 hours prior to imaging.

Seizure inductions

All mice used for seizure induction, including controls, were single-housed following intracranial injections. To ensure adaptation, mice were transferred to fresh housing with access to standard chow and water at least three days before behavioral experiments. They remained in the same cage throughout the study. All procedures were conducted during the light cycle, and careful handling was employed to minimize stress.

For intraperitoneal (IP) injections, mice were briefly anesthetized with 3.5% isoflurane. To induce transgene expression, all mice first received an IP injection of doxycycline HCl (4 mg/kg in saline) and were returned to their housing. After a 30-minute interval, mice were re-anesthetized under 3.5% isoflurane and administered an IP injection of either saline (200–250 μL) or kainic acid (KA) (20 mg/kg in saline, pH 7.4). In the seizure group, if no behavioral seizure symptoms were observed within one hour of KA injection, an additional 5 mg/kg dose of KA was administered.

Following KA or saline injection, mice were continuously recorded for one hour using a webcam positioned above the cage to capture behavioral seizure activity. Animals that did not recover from seizures within two hours received a subcutaneous injection of diazepam (10 mg/kg in saline) and were closely monitored until full recovery. All mice were returned to their standard housing overnight and imaged 24 hours after doxycycline administration.

Histological analysis

Tissue collection: Following the imaging session, animals were perfused transcardially with 15 mL of PBS, followed by 15 mL of 10% formalin solution. Brains were carefully resected and incubated in 10% formalin at 4°C on a rotator for 12–24 hours. The samples were then transferred to 30% sucrose for 48 hours to ensure cryoprotection before embedding in OCT compound and freezing at −80°C for long-term storage.

Frozen tissue cryosectioning: Frozen brain tissue was secured onto a cryosectioning chuck and sectioned at 60 μm thickness, spanning AP -1.2 mm to AP -3.5 mm relative to bregma. Slices were collected into PBS and stored at 4°C in the dark for up to two weeks before further processing.

Immunohistochemistry staining: All PBS wash steps and incubations were done on an orbital shaker. Tissue sections were washed once in 1X PBS to remove residual OCT and fixative. Sections were then incubated in freshly prepared blocking buffer containing 5% goat serum and 0.5% triton X-100 in 1X PBS for 60 minutes at room temperature. Sections stained with Cleaved Caspase 3 (Casp3) used a blocking buffer containing 10% Donkey serum, 2% BSA and 0.5% triton X-100 in 1X PBS. Following blocking, slides were washed three times in 1X PBS for 5 minutes each. Sections were then incubated overnight at 4°C in the dark with the primary antibody solution containing 1% BSA and 0.3% triton X-100 in 1x PBS. The Casp3 primary antibody dilution buffer contained 10% Donkey serum, 2% BSA and 0.3% triton X-100 in 1X PBS. The next day, slices were washed three times in 1X PBS before incubation with the secondary antibody solution containing 1X PBS for 2 hours at 4°C in the dark. After secondary staining, sections were washed three times in 1X PBS for 5 minutes each. Where applicable, slices were stained with DAPI (2.5 μg/mL) for 10 minutes, followed by three 5-minute wash in 1X PBS. For mounting, 200 μL of mounting media (Electron Microscopy Sciences, Catalog #17985-11) was added to each slide before carefully sealing with a coverslip. Slides were allowed to dry before imaging and were protected from light throughout all staining steps to preserve fluorescence.

The following antibodies were used for staining: NeuN (Abcam, Catalog #ab104225) at 1:1000 dilution, GFAP (Cell Signaling Technology, Catalog #12389S) at 1:250 dilution, Casp3 (Cell Signaling Technology, Catalog #9661S) at 1:400 dilution, Alexa-fluor 647 secondary (Abcam, Catalog #ab150079) at 1:1000 dilution, Alexa Fluor 405 (Abcam, Catalog # ab175651) secondary at 1:1000 dilution.

Microscopy imaging: Whole-slice imaging was performed using a 10X objective lens on a slide-scanning microscope. For imaging GFP, RFP, NeuN, and GFAP-positive cells, confocal imaging was conducted on an inverted laser scanning confocal microscope using a 20X objective lens. A z-stack scan was acquired, with each optical slice being 2 μm thick. For caspase-3-positive cell quantification, confocal imaging was performed using the same inverted laser scanning confocal

microscope with a 40X objective lens. A z-stack scan was acquired, with each optical slice being 1 μm thick.

Image analysis and cell counting: Slide-scanner images were analyzed using QuPath. To quantify fluorescence intensity and correlate it with BURST signal, a manual ROI was drawn unilaterally around the hippocampus on the injected side of the brain. The MFI of GFP, RFP, or iRFP670 within this ROI was used as the signal. On the contralateral side, a smaller ROI was drawn around the upper molecular layer of the dentate gyrus (DG) and the stratum lacunosum-moleculare (SLM) of CA1, regions that exhibited minimal iRFP670 expression. The MFI within this ROI was used as the background. Signal values were background-subtracted on a per-sample basis to account for slide-to-slide variability.

Only confocal images were used for cell counting, as detailed below. Before quantification, a 6 μm substack with strong expression and staining was selected in Fiji using the "Make Substack" function. Each channel was then exported in HDF5 format for further analysis. Pixel segmentation was performed on each image using Ilastik, and the segmented images were subsequently exported for analysis in Fiji.

To quantify GFP-, RFP-, and NeuN-positive cells, the HDF5 segmentation file was loaded into Fiji, and the segmentation was converted into a binary mask. To ensure that only cell nuclei were included in the analysis, an AND operation was performed between each mask and the DAPI mask using the Image Calculator tool. Co-expressing cells were identified by performing an additional AND operation between the relevant masks (e.g., GFP-DAPI and RFP-DAPI). Each resulting image was processed using the Watershed function to separate clustered objects. Finally, cell counting was performed using the Analyze Particles tool, with a threshold set to exclude objects smaller than 20 pixels.

To quantify cleaved caspase-3 positive cells, a Gaussian blur filter ($\sigma = 0.4$ μm) was applied to the corresponding channel to reduce noise. Cells with cleaved caspase-3 were then manually counted using the Cell Counter plugin in Fiji. Cell death was quantified by calculating the ratio of cleaved caspase-3 positive cells overlapping with GFP and RFP cells to the total number of GFP- and RFP-expressing cells in each image.

In vitro ultrasound imaging

In vitro BURST imaging sequence: Ultrasound imaging for *in vitro* experiments was performed using a Verasonics Vantage programmable ultrasound scanning system with an L22-14vX 128-

element linear array transducer (Verasonics). Image acquisition was conducted using previously published BURST scripts17. The transmit waveform was set to a frequency of 15.6 MHz, with a 67% intra-pulse duty cycle and seven half-cycle transmits. The BURST pulse sequence consisted of an initial low-pressure frame (transducer voltage: 1.6 V; peak positive pressure: 0.4 MPa) followed by 45 high-pressure frames (transducer voltage: 15 V; peak positive pressure: 3.6 MPa). The programmable transmit focus was set to 8 mm to align with the fixed elevation focus of the transducer. All images were captured in AM mode.

In vitro BURST image processing: All *in vitro* BURST images were reconstructed using a previously established temporal-template unmixing algorithm across individual pixel locations in the frame stack17. Normalized signal-to-background ratio (SBR) was defined as the average BURST signal in the well containing a sample of interest divided by the average signal inside a noise ROI drawn adjacent to the well and inside the phantom.

In all images where decibel (dB) units are used, dB is defined as:

$dB = 20 \log10(signal)$

In vivo image acquisition with 2D linear array

For all images captured using the 2D linear array, an initial low-voltage power Doppler image (5V) was acquired to find the desired imaging plane. This voltage was selected based on preliminary experiments to prevent GV collapse. Once the imaging plane was established, a BURST image was acquired, followed by a high-voltage power Doppler image (20V). All Doppler images presented in the manuscript correspond to the 20V power Doppler acquisitions.

In vivo BURST imaging sequence with 2D linear array: The same Verasonics Vantage system and L22-14vX transducer used for *in vitro* experiments was employed for *in vivo* imaging. The BURST pulse sequence began with a single low-pressure frame (transducer voltage: 1.6 V), followed by 16 high-pressure frames (transducer voltage: 20 V). To capture the entire depth of the brain, multiple transmit foci were used, with a BURST image acquired at each focus. These images were then summed to generate a composite BURST image. All images were captured in AM mode.

Doppler imaging with 2D linear array: Power Doppler images of cerebral blood volume (CBV) were acquired at 15.625 MHz. The imaging protocol utilized a pulse sequence consisting of 15 tilted plane waves, varying from −14° to 14°, with a pulse repetition frequency of 500 Hz. A total

of 200 coherently compounded frames were acquired. A singular value decomposition (SVD) clutter filter (cutoff = 40) was used to create the final power Doppler image showing CBV in the whole imaging plane42. Doppler imaging sequence with matrix array was based on previously established methods20.

In vivo image acquisition with matrix array

For volumetric BURST imaging, we used a modified version of Takoyaki BURST20 with a 15 MHz matrix array probe (Vermon), which transmits multiple focused beams and receives corresponding signals using a single group of 32 x 8 elements without parallel elements. Each volume image was acquired in AM mode. Therefore, 200 TX x 3 AM modes = 600 events were required to obtain one volume image. The input voltage to the matrix array transducer was set to 1.6 V for low-pressure pulses and at least 25V for the high-pressure pulses.

In vivo BURST image processing

Let $X_1, X_2, \dots, X_N$ be the sequence of N ultrasound images acquired following a pressure increase in the BURST scheme, with GV collapse occurring at the frame X_1. To incorporate prior knowledge of the GV collapse signal's temporal pattern, we computed the correlation between a template vector $Y = [1\ 0\ 0\ 0\ \dots\ 0] \in R^N$ and the temporal profile of each voxel. The correlation coefficient r for voxel $i \in \{1, \dots, k\}$, where k is the number of voxels per frame, was calculated as,

$$r^i = Corr(X^i, Y) = \frac{\sum_{n=1}^{N}(X_n^i - \bar{X}^i)(Y_n - \bar{Y})}{\sqrt{\sum_{n=1}^{N}(X_n^i - \bar{X}^i)^2 \sum_{n=1}^{N}(Y_n - \bar{Y})^2}}$$

where $\bar{X} = \sum_{n=1}^{N} X_n/N$ and $\bar{Y} = 1/N$ denote the temporal means of X and Y, respectively. To form the final BURST image, we retained only the voxels from the collapse frame X_1 whose correlation coefficients are above a threshold θ:

$$BURST = X_1 \odot 1(r > \theta)$$

where $\odot$ represents element-wise multiplication, and $1(\cdot)$ is the indicator function. Although the choice of threshold is arbitrary, its value can be selected based on how aggressively we wish to exclude background voxels that lack GVs. Assume there is no movement during image acquisition, voxels are independent (or images can be spatially downsampled so that spatial correlation is negligible), and each background voxel amplitude follows an i.i.d. Gaussian process. The amplitude of background voxel i can be expressed with random variables:

$$X^i_{background} \sim N(\mu^i, \sigma^i)$$

where μ is the mean amplitude, and σ is the standard deviation of the amplitude. Note that the superscript i implies that each background voxel may follow a different normal distribution. Given the independence of X and Y, and that at least one follows a univariate normal distribution, the sampling distribution of the correlation coefficient r is

$$f(r) = \frac{(1-r^2)^{\frac{N-4}{2}}}{B\left(\frac{1}{2}, \frac{N-2}{2}\right)}$$

where B is the Beta function[43,44]. Since this distribution is not dependent of the voxel amplitude parameters (μ^i and σ^i), all background voxels share the same sampling distribution of r. Instead of using the above formula directly, we can take advantage of its relationship to the t-distribution[43,44]:

$$t = r\sqrt{\frac{N-2}{1-r^2}} \quad \rightarrow \quad r = \frac{t}{\sqrt{N-2+t^2}}$$

where t follows a t-distribution with N-2 degrees of freedom. For 2D images, we chose $\theta = 0.7$ (N = 16), corresponding to a background rejection rate of 0.9987.

During 3D ultrasound image acquisition, GV collapse often spanned multiple frames. Suppose GVs collapse in frames $X_1, \ldots, X_a$ and we are confident there is no further collapse from X_b, where $a < b \leq N$. In this case, we computed a BURST image from each of $X_1, \ldots, X_a$ frames and sum them:

$$BURST = \sum_{j=1}^{a} BURST_j = \sum_{j=1}^{a} X_j \odot 1(r_j = Corr([X_j \ X_b \ X_{b+1} \ \ldots \ X_N], Y) > \theta)$$

where $Y = [1\ 0\ 0\ 0 \ldots 0] \in R^{N-b+2}$. We chose $\theta = 0.7036$ (N = 27, b = a+3 = 6), yielding a background rejection rate of 0.99991 for each $BURST_j$.

3.5 References

1 1.Ahrens, M. B., Orger, M. B., Robson, D. N., Li, J. M. & Keller, P. J. Whole-brain functional imaging at cellular resolution using light-sheet microscopy. Nat Methods 10, 413–420 (2013).
2. Prevedel, R. et al. Simultaneous whole-animal 3D imaging of neuronal activity using light-field microscopy. Nat Methods 11, 727–730 (2014).
3. Yoon, S. Y. et al. Quantitative, noninvasive, *in vivo* longitudinal monitoring of gene expression in the brain by co-AAV transduction with a PET reporter gene. Molecular Therapy Methods & Clinical Development 1, (2014).
4. Hochgräfe, K. & Mandelkow, E.-M. Making the Brain Glow: *In Vivo* Bioluminescence Imaging to Study Neurodegeneration. Mol Neurobiol 47, 868–882 (2013).
5. Maresca, D. et al. Biomolecular Ultrasound and Sonogenetics. Annual Review of Chemical and Biomolecular Engineering 9, 229–252 (2018).
6. Farhadi, A., Ho, G. H., Sawyer, D. P., Bourdeau, R. W. & Shapiro, M. G. Ultrasound imaging of gene expression in mammalian cells. Science 365, 1469–1475 (2019).
7. Hurt, R. C. et al. Genomically mined acoustic reporter genes for real-time *in vivo* monitoring of tumors and tumor-homing bacteria. Nat Biotechnol 41, 919–931 (2023).
8. Shivaei, S. et al. Non-invasive imaging of cell-based therapies using acoustic reporter genes. 2024.11.01.621111 Preprint at https://doi.org/10.1101/2024.11.01.621111 (2024).
9. Jin, Z. et al. Ultrasonic reporters of calcium for deep tissue imaging of cellular signals. 2023.11.09.566364 Preprint at https://doi.org/10.1101/2023.11.09.566364 (2023).
10.Deverman, B. E. et al. Cre-dependent selection yields AAV variants for widespread gene transfer to the adult brain. Nature Biotechnology 34, 204–209 (2016).
11.Chan, K. Y. et al. Engineered AAVs for efficient noninvasive gene delivery to the central and peripheral nervous systems. Nat Neurosci 20, 1172–1179 (2017).
12.Tabebordbar, M. et al. Directed evolution of a family of AAV capsid variants enabling potent muscle-directed gene delivery across species. Cell 184, 4919-4938.e22 (2021).
13.Dalkara, D. et al. *In Vivo*–Directed Evolution of a New Adeno-Associated Virus for Therapeutic Outer Retinal Gene Delivery from the Vitreous. Science Translational Medicine 5, 189ra76-189ra76 (2013).
14.Wang, J.-H., Gessler, D. J., Zhan, W., Gallagher, T. L. & Gao, G. Adeno-associated virus as a delivery vector for gene therapy of human diseases. Sig Transduct Target Ther 9, 1–33 (2024).
15.Choi, J.-H. et al. Optimization of AAV expression cassettes to improve packaging capacity and transgene expression in neurons. Mol Brain 7, 17 (2014).
16.Aschauer, D. F., Kreuz, S. & Rumpel, S. Analysis of Transduction Efficiency, Tropism and Axonal Transport of AAV Serotypes 1, 2, 5, 6, 8 and 9 in the Mouse Brain. PLOS ONE 8, e76310 (2013).
17.Sawyer, D. P. et al. Ultrasensitive ultrasound imaging of gene expression with signal unmixing. Nat Methods 18, 945–952 (2021).
18.Farhadi, A. et al. Genetically Encoded Phase Contrast Agents for Digital Holographic Microscopy. Nano Lett. 20, 8127–8134 (2020).
19.Schrunk, E., Dutka, P., Hurt, R. C., Wu, D. & Shapiro, M. G. Bioorthogonal Labeling Enables *In Situ* Fluorescence Imaging of Expressed Gas Vesicle Nanostructures. Bioconjugate Chem. 35, 333–339 (2024).
20.Lee, S., Wu, D., Malounda, D., Rabut, C. & Shapiro, M. G. Real-time volumetric imaging of cells and molecules in deep tissues with Takoyaki ultrasound. 2024.11.14.623368 Preprint at https://doi.org/10.1101/2024.11.14.623368 (2024).

21. Kawashima, T., Okuno, H. & Bito, H. A new era for functional labeling of neurons: activity-dependent promoters have come of age. Front. Neural Circuits 8, (2014).
22. Kawashima, T. et al. Functional labeling of neurons and their projections using the synthetic activity–dependent promoter E-SARE. Nature Methods 10, 889–895 (2013).
23. Sørensen, A. T. et al. A robust activity marking system for exploring active neuronal ensembles. eLife 5, e13918 (2016).
24. Kashihara, K. et al. Temporal pattern of AP-1 DNA-binding activity in the rat hippocampus following a kindled seizure. Neuroscience 80, 753–761 (1997).
25. Malnou, C. E. et al. Heterodimerization with Jun Family Members Regulates c-Fos Nucleocytoplasmic Traffic *. Journal of Biological Chemistry 282, 31046–31059 (2007).
26. Barth, A. L., Gerkin, R. C. & Dean, K. L. Alteration of Neuronal Firing Properties after *In Vivo* Experience in a FosGFP Transgenic Mouse. J. Neurosci. 24, 6466–6475 (2004).
27. Guenthner, C. J., Miyamichi, K., Yang, H. H., Heller, H. C. & Luo, L. Permanent Genetic Access to Transiently Active Neurons via TRAP: Targeted Recombination in Active Populations. Neuron 78, 773–784 (2013).
28. DeNardo, L. A. et al. Temporal evolution of cortical ensembles promoting remote memory retrieval. Nat Neurosci 22, 460–469 (2019).
29. Josselyn, S. A. & Tonegawa, S. Memory engrams: Recalling the past and imagining the future. Science 367, eaaw4325 (2020).
30. Liu, X. et al. Optogenetic stimulation of a hippocampal engram activates fear memory recall. Nature 484, 381–385 (2012).
31. Denny, C. A. et al. Hippocampal Memory Traces Are Differentially Modulated by Experience, Time, and Adult Neurogenesis. Neuron 83, 189–201 (2014).
32. Reijmers, L. G., Perkins, B. L., Matsuo, N. & Mayford, M. Localization of a Stable Neural Correlate of Associative Memory. Science 317, 1230–1233 (2007).
33. Matlashov, M. E. et al. A set of monomeric near-infrared fluorescent proteins for multicolor imaging across scales. Nat Commun 11, 239 (2020).
34. Morgan, J. I., Cohen, D. R., Hempstead, J. L. & Curran, T. Mapping Patterns of c-fos Expression in the Central Nervous System After Seizure. Science 237, 192–197 (1987).
35. Lévesque, M. & Avoli, M. The kainic acid model of temporal lobe epilepsy. Neurosci Biobehav Rev 37, 2887–2899 (2013).
36. Lashley, K. S. In search of the engram. in Brain Physiology and Psychology (eds. Evans, C. R. & Robertson, A. D. J.) 1–32 (University of California Press, 1950). doi:10.1525/9780520318267-001.
37. Rubin, A., Geva, N., Sheintuch, L. & Ziv, Y. Hippocampal ensemble dynamics timestamp events in long-term memory. eLife 4, e12247 (2015).
38. Attardo, A. et al. Long-Term Consolidation of Ensemble Neural Plasticity Patterns in Hippocampal Area CA1. Cell Reports 25, 640-650.e2 (2018).
39. Roy, D. S. et al. Brain-wide mapping reveals that engrams for a single memory are distributed across multiple brain regions. Nat Commun 13, 1799 (2022).
40. Lakshmanan, A. et al. Acoustic biosensors for ultrasound imaging of enzyme activity. Nat Chem Biol 16, 988–996 (2020).
41. Hurt, R. C. et al. Directed Evolution of Acoustic Reporter Genes Using High-Throughput Acoustic Screening. ACS Synth. Biol. 13, 2215–2226 (2024).
42. Macé, E. et al. Functional ultrasound imaging of the brain. Nature Methods 8, 662–664 (2011).
43. Hotelling, H. New Light on the Correlation Coefficient and its Transforms. Journal of the Royal Statistical Society: Series B (Methodological) 15, 193–225 (1953).
44. John F Kenney. Mathematics Of Statistics Part Two. (1939).

3.6 Figures

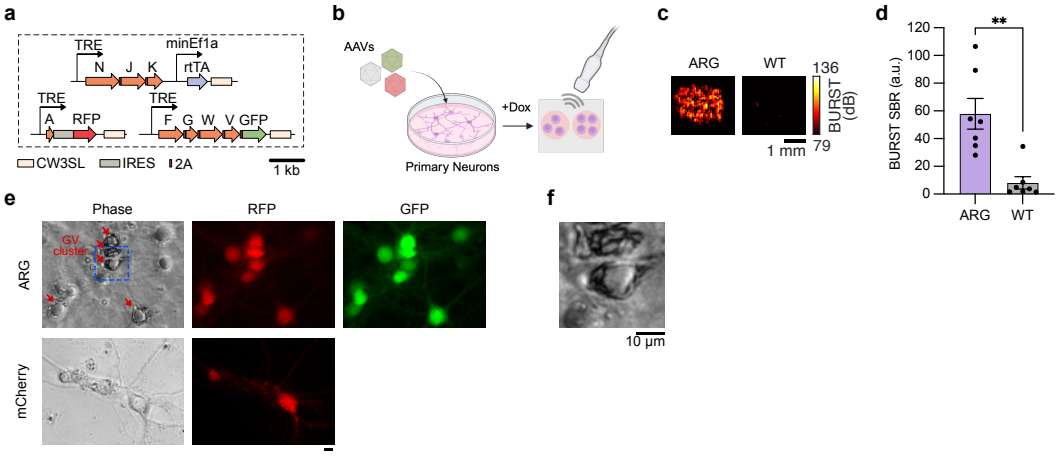

Figure 3-1: AAV-mediated delivery of the GV gene cluster into primary neurons.
a, Schematic of the 3-vector AAV system, with the structural gene gvpA encoded on a separate plasmid to enable stoichiometric tuning of its expression relative to assembly factors. **b,** Schematic of the experimental protocol for validating GV expression in cultured mouse embryonic neurons. Cultured neurons were induced with doxycycline every 24 hours, for 72 hours prior to dissociation and ultrasound imaging in agarose phantoms. **c,** Representative BURST images of neurons expressing ARGs (left) and wild-type (WT) neurons (right). **d,** Quantification of the BURST signal-to-background ratio (SBR) in wells containing GV-expressing neurons compared to WT cells. Error bars represent mean ± s.e.m., n = 7 biological replicates. Each data point is the arithmetic mean of n = 2 technical replicates. Welch's t test, p = 0.0031. **e,** Phase contrast (left) and fluorescence (right) images of neurons transduced with GV-expressing AAVs or mCherry-expressing AAVs. Arrows point at visible GV clusters, appearing as dark structures inside the cell, under phase contrast microscopy. **f,** Magnified view of the cell outlined the blue box in (e), showing visible GV clusters.

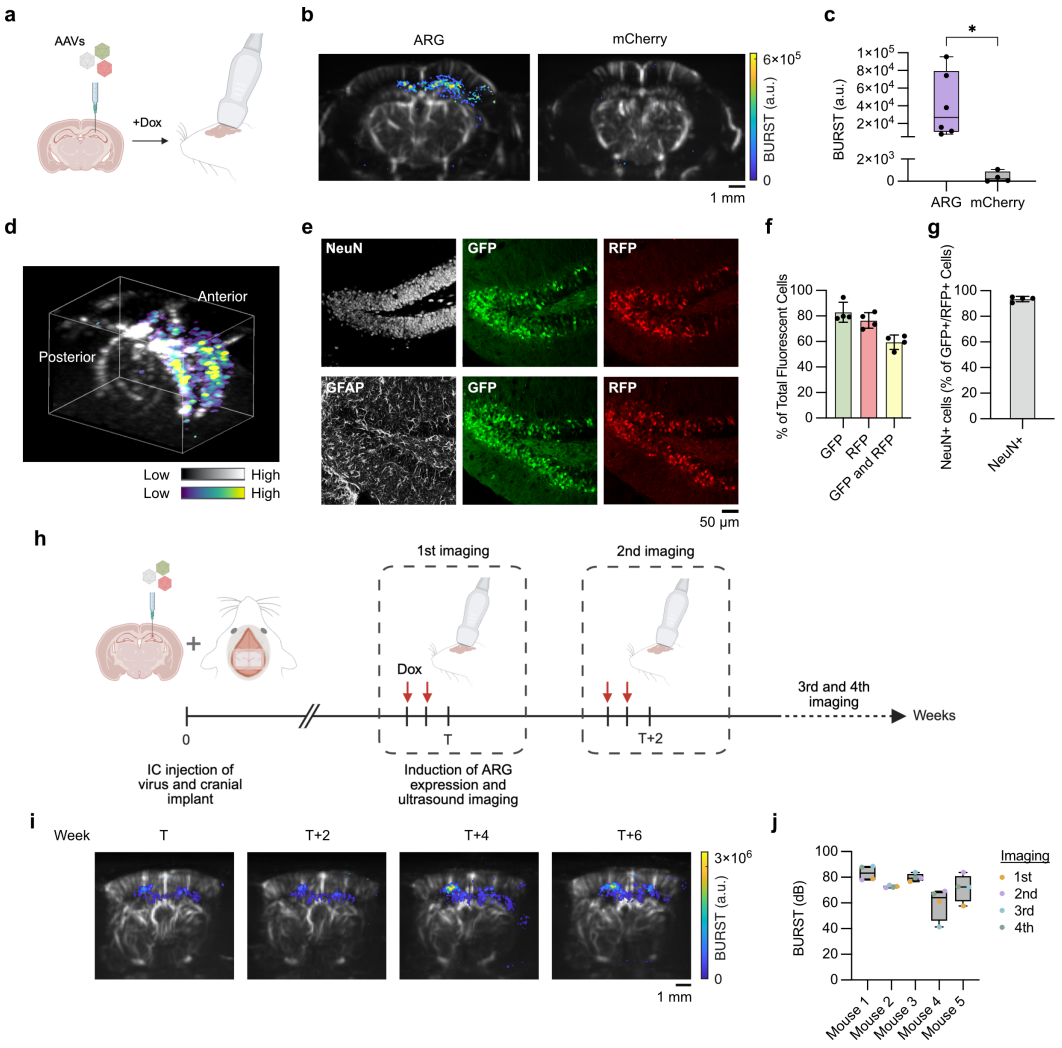

Figure 3-2: AAV-delivery and longitudinal imaging of GV-expression in the mouse brain.
a, Schematic of the experimental approach, in which a mix of the three ARG-encoding AAVs is intracranially injected into the hippocampus. GV expression is induced for 72 hours, and the hippocampus is imaged through a cranial window. **b**, Representative BURST images (colormap) overlaid on Doppler images (grayscale) of the mouse brain injected with ARG-encoding AAVs or a constitutively mCherry-expressing AAV. **c**, Quantification of the BURST signal in the brains of mice injected with ARG-encoding AAVs (n = 6) or mCherry-expressing AAVs (n = 3). **d**, Volumetric BURST imaging of the brain using Takoyaki imaging, overlaid on volumetric Doppler images. Anterior and posterior directions of the brain are indicated. **e**, Representative histological images of fluorescence expression in the dentate gyrus (DG) of ARG-injected mice, with neuronal (NeuN) and astrocyte (GFAP) staining. **f**, Quantitative analysis of fluorescent cell populations in the DG, showing the percentages of GFP+, RFP+, and GFP+/RFP+ cells (n = 922 fluorescent cells counted across n = 2 mice). **g**, Quantitative analysis of fluorescent cells in the DG that are neuronal (NeuN+) (n = 563 fluorescent cells counted across n = 2 mice). **h**, Schematic of the longitudinal imaging experiment. Following intracranial injection of the AAVs, an acoustically transparent window is placed on the brain. GV expression is induced for 48 hours, followed by imaging and GV collapse. Doxycycline induction and imaging are repeated every two weeks for a total of four cycles. **i**, Representative ultrasound images of approximately the same anterior-posterior plane over the span of 4 imaging rounds. **j**, Quantification of BURST signal in the same imaging plane across four sessions in n = 5 mice. For (c) and (j), the line in the middle represents the median, the box spans the 25th to 75th percentiles, and the whiskers indicate the minimum and maximum values. In (f) and (g), the line represents the mean and error bars indicate the s.e.m.

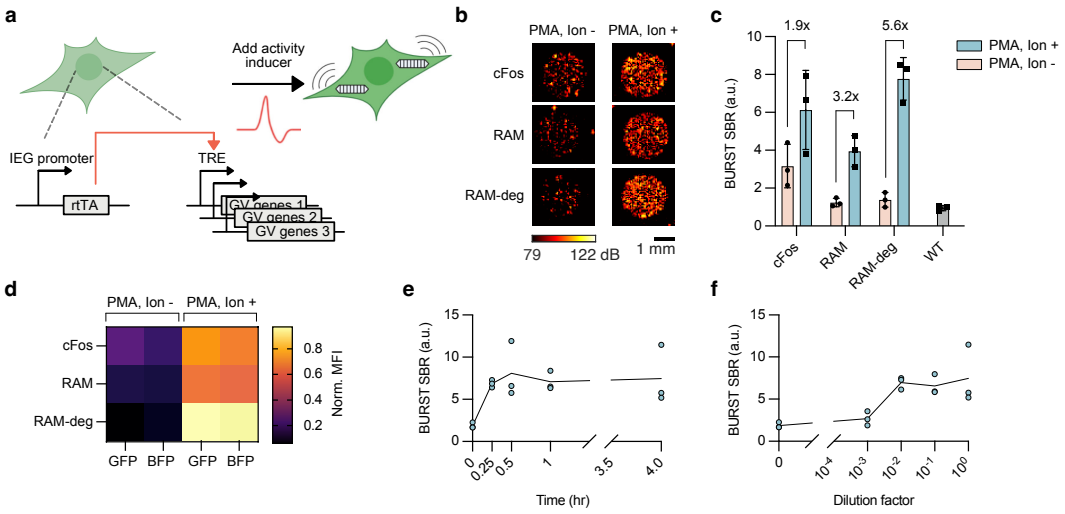

Figure 3-3: Immediate-Early Gene Promoters Enable Activity-Dependent GV Expression in HEK293T Cells.

a, Schematic of the plasmid design and experimental approach for testing variants of IEG-induced GVs. rtTA is expressed under an IEG promoter (either cFos or RAM), which activates the transcription of GV genes in the presence of doxycycline. To reduce the half-life of rtTA, a degron-linked version (RAM-deg) was also tested. These variants were packaged into a lentiviral backbone and transduced into HEK293T cells. Activity was induced by adding PMA and ionomycin to the culture for 4–6 hours unless noted otherwise. Cells were imaged 24 hours post-induction. **b**, Representative BURST images of HEK293T cells in their resting (PMA, Ion -) or active (PMA, Ion +) state with different IEG-induced GV variants. **c**, Quantification of BURST signal and fold change in HEK cells expressing different IEG variants compared to WT cells. **d**, Mean fluorescence intensity (MFI) of resting and activity-induced cells expressing different IEG variants, normalized to the maximum intensity for each fluorescence channel. **e**, BURST signal in RAM-deg-expressing cells induced for varying durations. **f**, BURST signal in RAM-deg-expressing cells treated with serial dilutions of the PMA and ionomycin mix. Error bars represent mean ± s.e.m. n = 3 biological replicates. Each data point represents the arithmetic mean of n = 2 technical replicates.

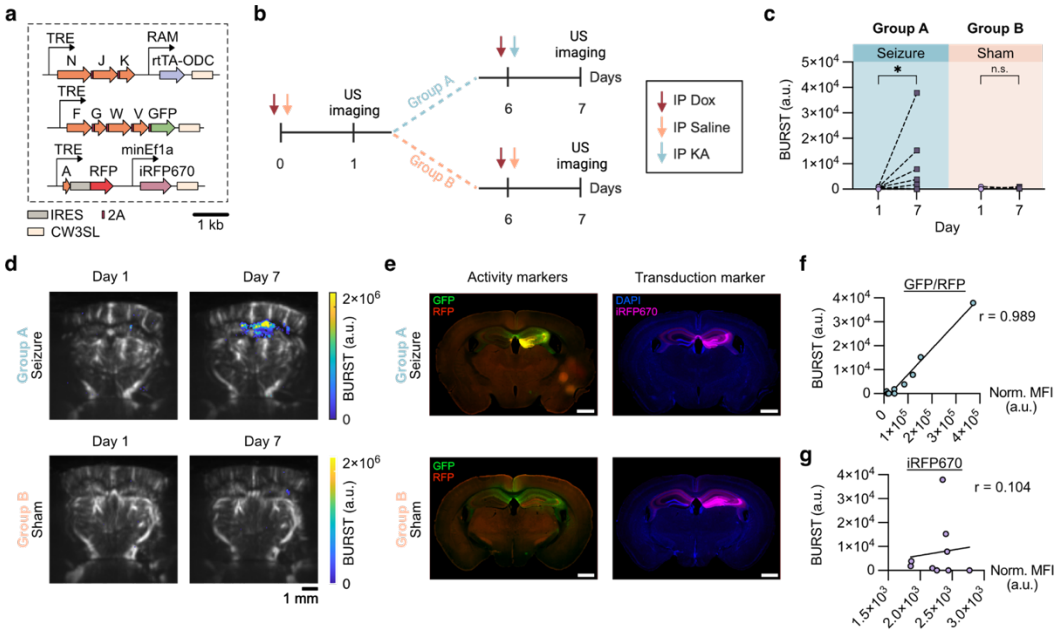

Figure 3-4: IEG-induced GV expression tracks changes in neuronal activity caused by seizures.
a, Schematic of the AAV design for IEG-induced GV expression using the RAM-deg promoter variant. A constitutive fluorophore, iRFP670, was included on the gvpA construct to account for variability in transduction efficiency. **b,** Experimental timeline for seizure induction and activity imaging. Mice were imaged at two time points: day 1 (baseline), following IP injections of doxycycline (Dox) and saline; and day 7, following either kainic acid and Dox (Group A) or a second saline and Dox injection (Group B). **c,** Quantification of BURST signal in the hippocampus for Group A (n = 8 mice) and Group B (n = 4 mice), as described in (b). Each line represents an individual mouse. Group A mice that did not exhibit an increase in fluorescence despite receiving KA were excluded from the significance test. Ratio-paired t test, p (Group A) = 0.003, p (Group B) = 0.284. Significance levels: *p ≤ 0.5, n.s. p > 0.5. **d,** Representative ultrasound images from Group A and Group B mice showing activity-induced BURST signal in the hippocampus. **e,** Fluorescence images of histological sections from the same mice shown in (d), taken at matched anterior–posterior planes (±0.3 mm). Left column: GFP and RFP fluorescence driven by the IEG promoter. Right column: constitutive iRFP670 expression and DAPI staining. **f,** Correlation between BURST signal and fluorescence signal from histological sections. Multiplied MFI (Mult. MFI) is defined as the product of GFP and RFP channel mean fluorescence intensities. Pearson r = 0.72, p (two-tailed) = 0.0457, n = 8 mice. **g,** constitutive iRFP670 fluorescence from histological sections. Pearson r = 0.104, p (two-tailed) = 0.79, n = 8 mice.

3.7 Supplementary Figures

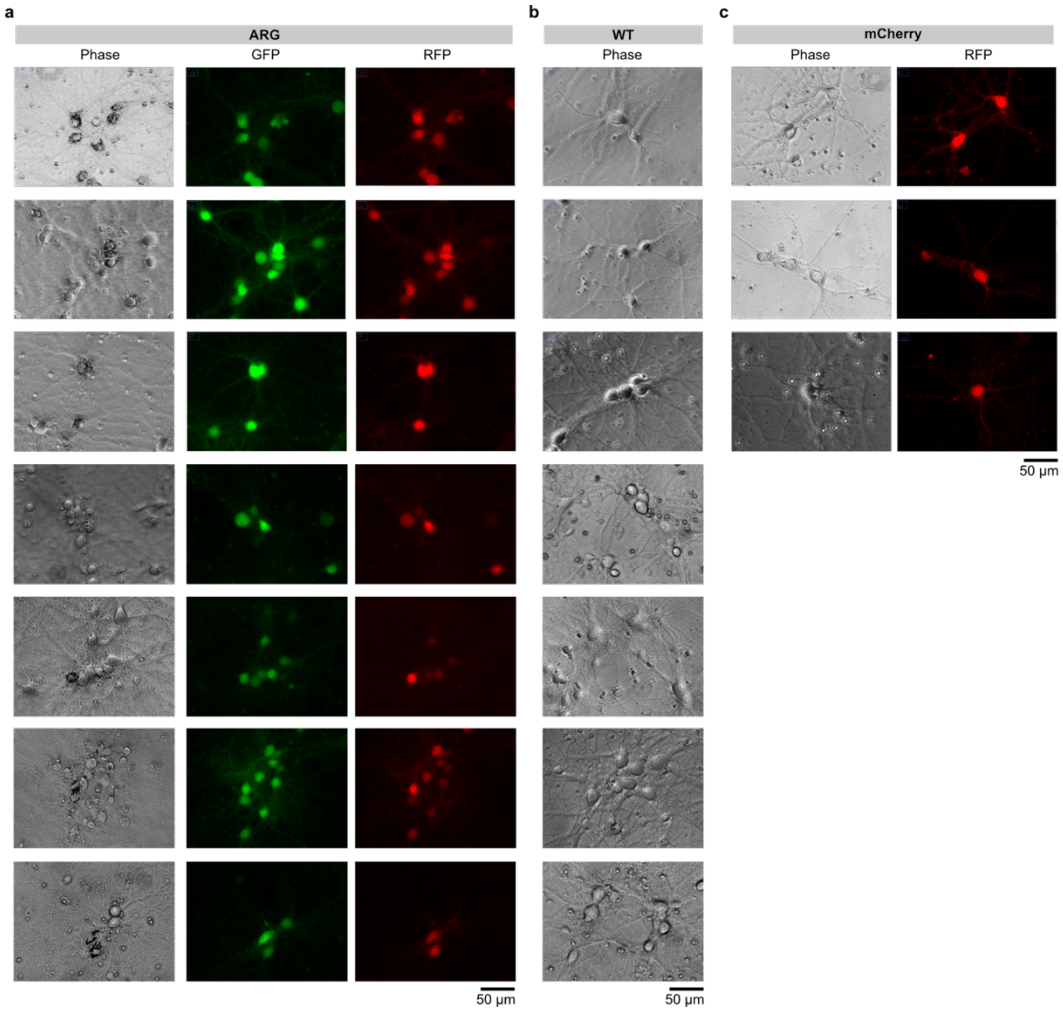

Figure 3-S1: Fluorescence microscopy of GV-expressing and control neurons.
a, Representative phase contrast, GFP, and RFP fluorescence images of primary mouse neurons transduced with the ARG AAV system. Cluster of GVs are present in cells with strong co-expression of GFP and RFP. **b,** Phase contrast images of wild-type (WT) neurons not transduced with AAVs, showing normal cell morphology. **c,** Representative phase contrast and RFP fluorescence images of neurons transduced with a constitutively expressing mCherry AAV. Cells show diffuse cytoplasmic expression of mCherry without clustered structures present in phase. Scale bars, 50 µm.

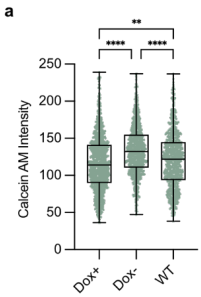

Figure 3-S2: Metabolic state of GV expressing neurons.
a, Calcein AM staining of primary cultured neurons transduced with ARG-expressing AAVs. Cells were either induced with doxycycline (Dox$^+$), left uninduced (Dox$^-$), or left non-transduced (WT). n = 1,064 (Dox$^+$), n = 820 (Dox$^-$), n = 760 (WT) individual cells counted.

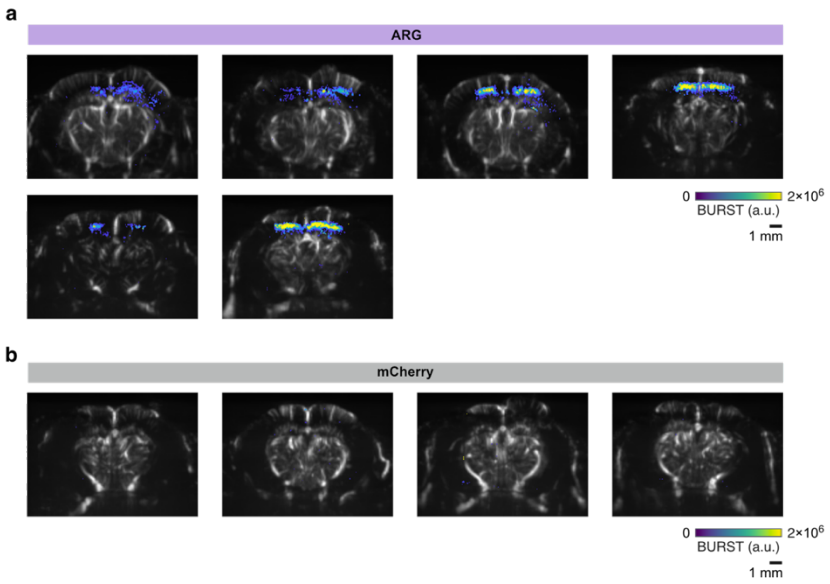

Figure 3-S3: Ultrasound imaging of GV-expressing and mCherry-expressing brains following intracranial AAV delivery.
Representative BURST images (colorbar) of brains injected with **a,** the GV-expressing three vector AAVs or **b,** injected with a mCherry-expressing AAV, overlaid on top of Doppler images (grayscale). Each image is from a different mouse. The plane closest to the injection site, as determined by the Doppler image, and with the strongest BURST signal was selected from each mouse.

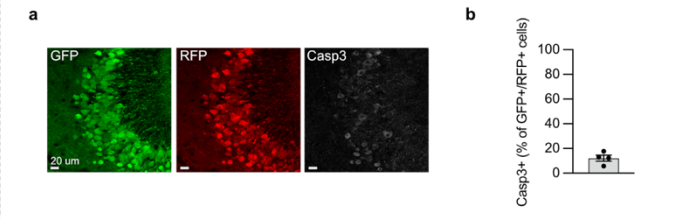

Figure 3-S4: Assessment of cell viability in GV-expressing mouse brains.
a, Representative fluorescence images of the CA3 region in a GV-expressing brain at the injection plane (AP –2.1 mm), showing GFP and RFP expression alongside cleaved caspase-3 (Casp3) staining. CA3 was the hippocampal subregion with the highest observed level of cell death. **b,** Quantification of Casp3$^+$ cells as a percentage of GFP$^+$ and RFP$^+$ cells (n = 445 fluorescent cells across n = 4 mice). Data are presented as mean ± s.e.m. Scale bar = 20 μm.

a

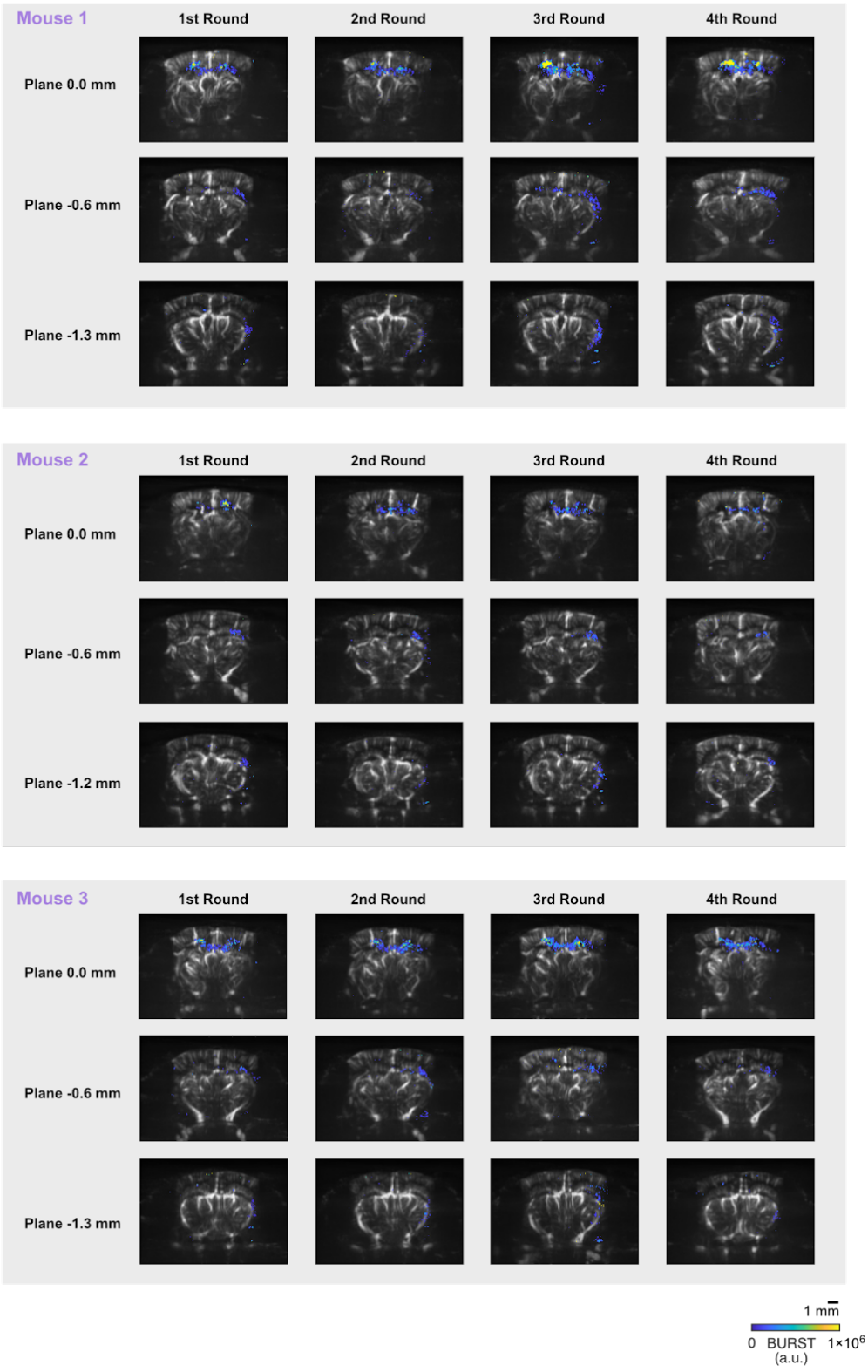
Mouse 1
1st Round
2nd Round
3rd Round
4th Round
Plane 0.0 mm
Plane -0.6 mm
Plane -1.3 mm
Mouse 2
1st Round
2nd Round
3rd Round
4th Round
Plane 0.0 mm
Plane -0.6 mm
Plane -1.2 mm
Mouse 3
1st Round
2nd Round
3rd Round
4th Round
Plane 0.0 mm
Plane -0.6 mm
Plane -1.3 mm
1 mm
0 BURST 1×10^6
(a.u.)

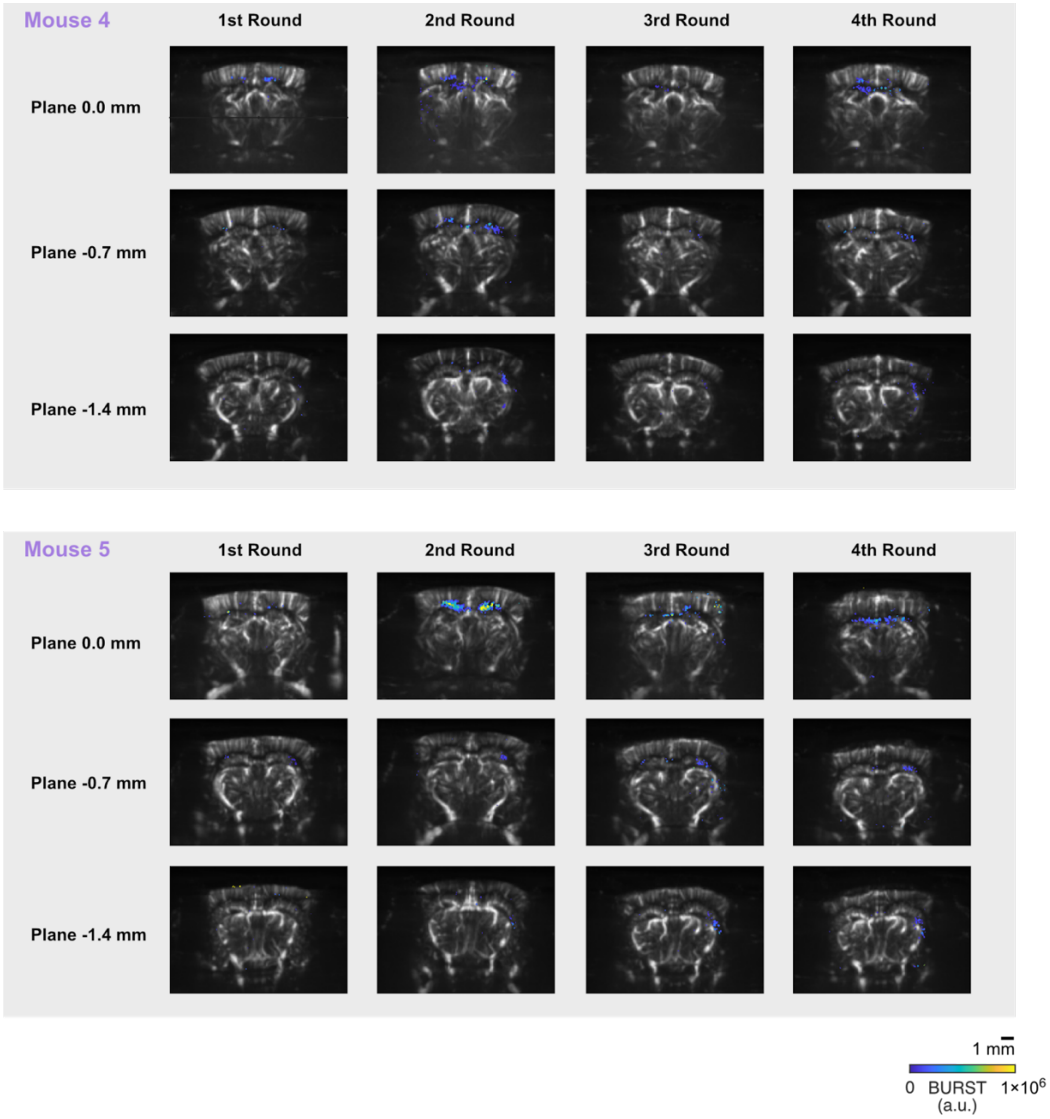

Figure 3-S5: Ultrasound imaging of repeated ARG expression in the brain.
a, Ultrasound images of repeated ARG expression in mice implanted with an acoustically transparent cranial window. Mice received doxycycline for 48 hours prior to each imaging session, with induction-imaging cycles spaced two to three weeks apart. For quantification, the imaging plane with the strongest BURST signal from the first session was used for all timepoints. BURST images are shown in color and overlaid on grayscale Doppler anatomical images. n = 5 mice.

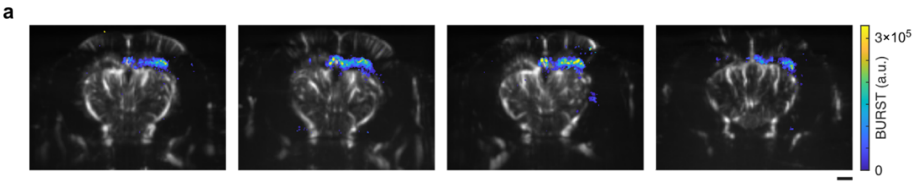

Figure 3-S6: Co-expression of a constitutive fluorophore with Tet-inducible *gvpA* does not affect ARG expression in the hippocampus.
a, Representative ultrasound images of the hippocampus from mice injected with an AAV encoding a Tet-inducible *gvpA* and a constitutive iRFP670 fluorophore (as in Fig. 3-4a), along with the two AAVs encoding assembly factors (as in Fig. 1a). BURST signal is shown in color and overlaid on grayscale Doppler images. n = 4 mice. Scale bar, 1 mm.

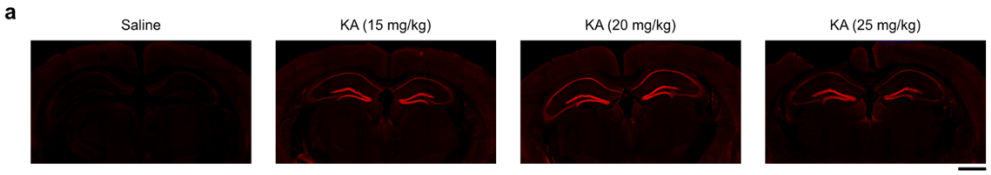

Figure 3-S7: Systemic kainic acid injection induces cFos expression in the hippocampus.
a, Representative images of cFos immunostaining in coronal brain sections from mice injected intraperitoneally (IP) with either saline or varying doses of kainic acid (KA). Mice were sacrificed 30 minutes after injection. Scale bar, 1 mm.

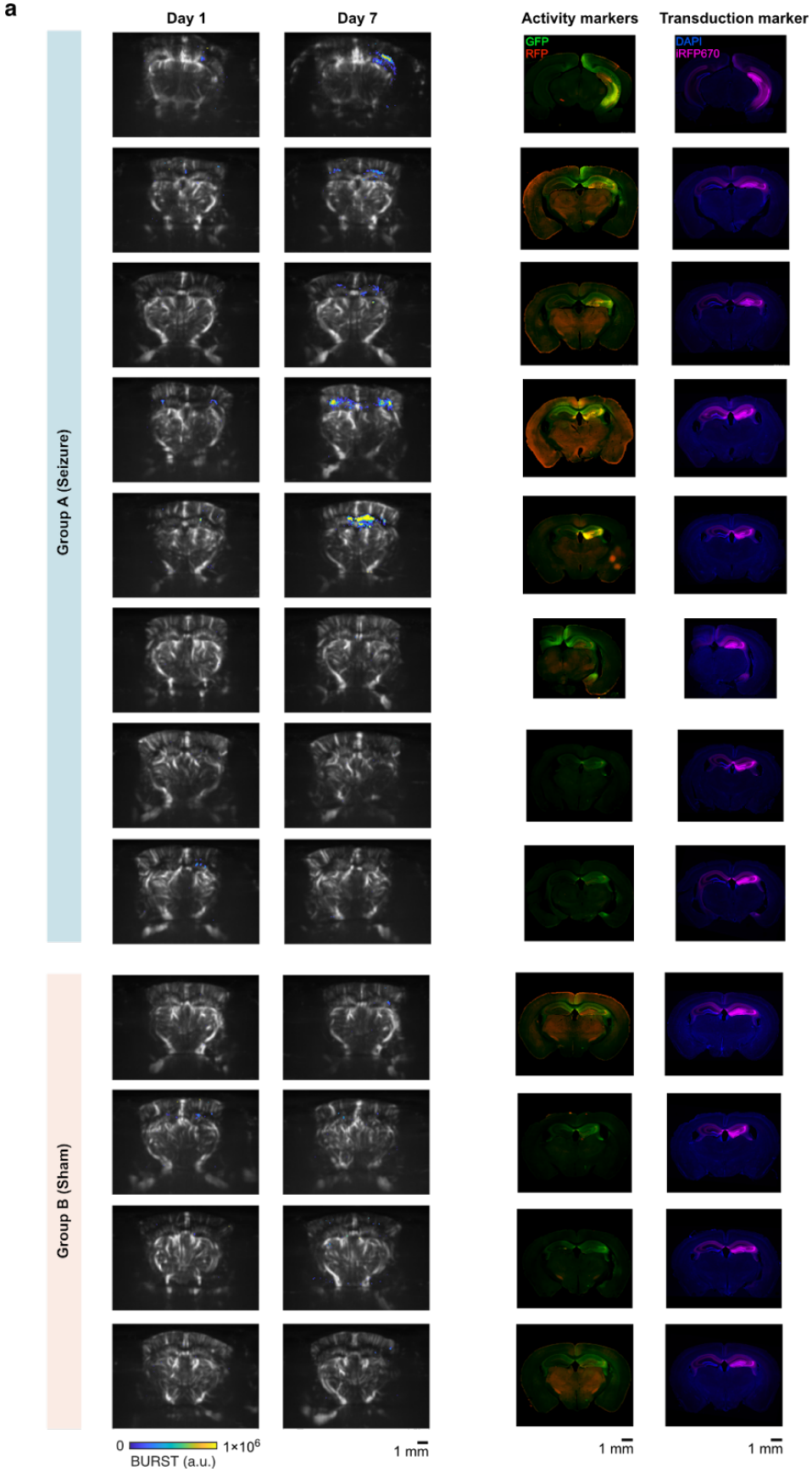
a
Day 1
Day 7
Activity markers
Transduction marker
GFP
RFP
DAPI
iRFP670
Group A (Seizure)
Group B (Sham)
0
1×10^6
BURST (a.u.)
1 mm
1 mm
1 mm

Figure 3-S8: Ultrasound and fluorescence images of reporter expression in mice with and without induced seizures.

a, Representative ultrasound and histological images from Group A (seizure) and Group B (sham) mice. Left panels: BURST images (colormap) overlaid on grayscale Doppler anatomical images acquired on day 1 (baseline, post-Dox/saline) and day 7 (post-Dox/KA or Dox/saline). Right panels: GFP and RFP fluorescence showing IEG-driven reporter expression (activity markers), and iRFP670 (transduction marker) with DAPI staining. Several Group A mice (rows 6 to 8) displayed seizure behavior following KA injection but showed no significant increase in BURST signal on day 7, consistent with weak fluorescence expression. For Group A mice, representative imaging planes were selected based on proximity to the injection site and the strongest observed change in BURST signal. Scale bars, 1 mm.

3.8 Supplementary Material

Plasmid	**Usage**
pAAV-TRE-NJK-minEf1a-rtTA-CW3SL	3-vector AAV GV expression (vector 1)
pAAV-TRE-FGWV-GFP-CW3SL	3-vector AAV GV expression (vector 2)
pAAV-TRE-GvpA-mScarlet-CW3SL	3-vector AAV GV expression (vector 3)
pAAV-TRE-GvpA-mScarlet-mEf1a-emiRFP670-CW3SL	3-vector AAV GV expression (vector 3) with constitutive emiRFP670 expression
pAAV-TRE-NJK-RAM-rtTA-ODC-CW3SL	3-vector AAV GV expression (vector 1) with RAM promoter and degron-tagged rtTA
pAAV-Ef1a-mCherry	Constitutive mCherry expression
pLV-TRE3G-NJKF-cFos-rtTA	3-vector lentiviral GV expression (AF1) with cFos promoter
pLV-TRE3G-NJKF-RAM-rtTA	3-vector lentiviral GV expression (AF1) with RAM promoter
pLV-TRE3G-NJKF-RAM-rtTA-ODC	3-vector lentiviral GV expression (AF1) with RAM promoter and degron-tagged rtTA
pLV-TRE3G-GWV-mEGFP	3-vector lentiviral GV expression (AF2)
pLV-TRE3G-GvpA-IRES-BFP	3-vector lentiviral GV expression (*gvpA*)
pLV-TRE3G-mScarlet-Ef1a-rtTA-BFP	HEK-TRE cell line
pLV-Ef1a-rtTA-HygR-WPRE	HEK-TetON cell line
pCMVR8.74	Lentivirus packaging plasmid
pMD2.G	Lentivirus packaging plasmid

Table 3-T1: Genetic constructs used in the study.
Sources of genetic elements: *Anabaena flos. aquae* GV gene cluster on lentiviral backbone: M. G. Shapiro; cFos: pAAV-cFos-tTA-pA (Addgene #66794); CW3SL: pAAV-CW3SL-EGFP (Addgene #61463), RAM and ODC: pAAV-RAM-d2TTA::TRE-FLEX-MCS-WPRE-pA (Addgene #84467); emiRFP670: pemiRFP670-N1 (Addgene #136556); pAAV-Ef1a-mCherry (Addgene #114470); Lentivirus packaging plasmids: pCMVR8.74 (Addgene #22036), pMD2.G (Addgene #12259).